Did eustatic sea-level control deep-water systems at Milankovitch and timescales?: An answer from Quaternary Pearl River margin

Kun Qi [a,b], Chenglin Gong [a,b,*], Kelly Fauquembergue [c], Yang Zhou [d]

[a] State Key Laboratory of Petroleum Resources and Prospecting, China University of Petroleum (Beijing), Beijing 102249, China
[b] College of Geosciences, China University of Petroleum (Beijing), Beijing 102249, China
[c] UMR CNRS 5805 EPOC, Université de Bordeaux, Bâtiment B18, 33615 Pessac Cedex, France
[d] Guangzhou Marine Geological Survey, Key laboratory of Marine Mineral Resources of Ministry of Natural Resources of the P. R. China, Guangzhou 510760, China

ARTICLE INFO

ABSTRACT

As one of the most important forcing factors, sea level fluctuations exert a major influence on deep-water depositional processes, however, it is still not well understood how they control the evolution of the specific deep-water system over different timescales. For relatively longer (1 My) and shorter (100 Ky) timescales, we characterize deep-water sedimentary records on the Pearl River margin using seismic and borehole data, and then compare them with the contemporaneous sea-level curve to exam the varied roles sea levels have played in impacting the development of the deep-marine system. Results indicate that over both the 1 My-scale and the 100 Ky-scale, the studied deep-water system shows systematic variations that are strongly suggested to arise from the modulation of sea levels. Specifically, over the 1 My-scale, facies and depocenters of the deep-water system all show significant changes. Large fan lobes (consisting of both turbidites and mass-transport deposits) with more distal depocenters likely correspond with low-amplitude and high-frequency sea level fluctuations and slightly rising shelf edge trajectories, whereas smaller turbidite fan lobes with more proximal depocenters likely reflect high-amplitude and low-frequency sea level fluctuations and steeply rising shelf-edge trajectories. In contrast, within the 100 Ky-scale of a glacial-interglacial cycle, the composition of deep-water deposits also shows significant variations. Coarser-grained deposits with higher organic carbon (TOC) content and lower calcium carbonate ($CaCO_3$) content are interpreted to reflect periods of glacial sea-level lowstand, whereas finer-grained sediments having lower TOC and higher $CaCO_3$ content reflect interglacial sea-level highstand. Moreover, the spectrum characteristics of these constituent curves are very similar to those of contemporaneous sea levels, reflecting Milankovitch climatic forcings and further validating the tight coupling between sea-level stands and sediment compositions. These correlations between sedimentary records and sea level behaviors suggest that it was mainly a long-term change in the amplitude and frequency of eustatic cycles that controlled the overall architecture of the deep-water system, whereas it was shorter term, changing sea-level stands that played a role and impacted the deep-water sediment composition.

© 2022 Elsevier B.V. All rights reserved.

1. Introduction

As the largest sedimentary bodies in the oceans, deep-water sedimentary systems not only contain relatively complete records of sediment flux from land to sea, constituting archives of the past continental and marine environments (Covault et al., 2010; Talling et al., 2015; Romans et al., 2016), they also have enormous hydrocarbon potential and are frequently surveyed by the hydrocarbon industry (Mayall et al., 2006; Weimer and Slatt, 2007; Covault et al., 2017).

Understanding of the forcings that govern the emplacement and development of those systems is therefore a matter of high scientific and societal interest.

Early sequence stratigraphy models emphasized that during the periods of falling sea level and lowstands the terrestrial sediments are delivered to shelf-margin staging areas, giving rise to the formation of deep-water systems (Vail et al., 1977; Mitchum, 1985; Van Wagoner et al., 1990). However, recent works on both ancient (Carvajal and Steel, 2006; Castelltort et al., 2017) and modern systems (Romans et al., 2009; Normark et al., 2009; Covault and Graham, 2010) have demonstrated that shelf bypass and the associated formation of sediment gravity-flow systems can also occur during rising and highstand of sea level when facilitated by a steep and narrow shelf, high sediment

* Corresponding author at: State Key Laboratory of Petroleum Resources and Prospecting, China University of Petroleum (Beijing), Beijing 102249, China.
  E-mail address: chenglingong@cup.eud.cn (C. Gong).

supply, and/or the presence of shelf-penetrating canyons (Khripounoff et al., 2009; Vangriesheim et al., 2009; Covault et al., 2010; Jorry et al., 2011; Sweet and Blum, 2016; Picot et al., 2019; Peng et al., 2021; Peng, 2021). Nevertheless, sea level fluctuations are still considered to be a primary driving mechanism for the formation of deep-water systems along passive and other types of margins (Galloway, 1989; Sydow and Roberts, 1994; Porębski and Steel, 2003, 2006), especially during icehouse periods dominated by high eustasy amplitude and frequency, such as the Quaternary (Sømme et al., 2009; Gong et al., 2016a, 2016b).

In general, previous studies have outlined the importance of sea-level controls on deep-water systems at different timescales. For example, for long timescale of millions of years, apart from the conventional discussions on the occurrence time of deep-water systems within sea-level cycles (Posamentier et al., 1992; Clift et al., 2008; Piper and Normark, 2009; Catuneanu, 2020), the sea-level influence on architecture evolution of submarine systems has also been paid much attention (Lopez, 2001; Picot et al., 2016; Zhang et al., 2018). Over the relatively short timescale of tens of thousands of years, core-based characterization of deep-water deposits and the analysis of sediment partitioning to deep water by sea-level forcings have also been discussed by an increasing number of works (Fauquembergue et al., 2019; Jiwarungrueangkul et al., 2019; Li et al., 2019). However, we note that those works only emphasis the development of deep-water systems and their sea-level control within a specific timescale. The emplacement of deep-marine deposits at both long and short timescales for the same system still needs much work, especially considering sea-level changes at different timescales may play varied roles on the same system.

Taking the Quaternary Pearl River margin at the northern South China Sea as the study object, we aim to explore the growth of the deep-water system as a function of sea-level changes at two different timescales. Firstly, we integrate 3D seismic and borehole data to conduct detailed characterization of submarine deposits. These new results provide details about the evolution of the deep-water system through time and build upon previous work on the characterization of shelf-edge deltas and unidirectionally migrating canyons on the Pearl River margin (Gong et al., 2016b; Gong et al., 2018; Gong et al., 2019). Then, through relating those deep-water sedimentary records to the contemporaneous eustatic sea-level curve, varied roles sea levels have played in modulating the deposition of the deep-water system are examined.

2. Geological background of the study area

2.1. Pearl River margin

The study area is located in the Pearl River Mouth Basin, which occupies an area of 1.75×10^5 km² and belongs to the central part of the northern South China Sea margin (Fig. 1A). The basin initiated as an elongated rift at 59 Ma, with two main stages of tectonic evolution, namely a Paleocene to Oligocene synrift stage and a Miocene to Quaternary postrift stage (Ru and Pigott, 1986; Franke et al., 2011; Zhao et al., 2016). Since 23.8 Ma, that northern continental margin of the South China Sea has a prominent shelf-slope-basin physiography, into which the long-term active, Pearl River fluvial system debouched (Gong et al., 2013; Zhuo et al., 2015; Gong et al., 2018; Lin et al., 2018a, 2018b). Offshore of the Pearl River mouth and on the upper continental slope, a canyon system, named Shenhu Submarine Canyon Group, connects the continental shelf and deep-sea basins (Fig. 1B) (Zhu et al., 2010; Ding et al., 2013; Lin et al., 2018a, 2018b; Su et al., 2020). The present work focuses on the deep-water system deposited within the last 1 My, which belong to the youngest and uppermost level of the postrift supersequence. During that period, the "Dongsha Tectonic Movement" was the most important neotectonic activity in the northern South China Sea (Li et al., 1999; Yao, 1999). It was caused by the convergence between the South China Sea and Philippine Sea plates and

primarily expressed as the uplift of the Dongsha Rise, the formation of NWW-trending fault systems, and large-scale thermal fluid movement (Yao and Yang, 2008; Zhao et al., 2012). However, it should be noted that those tectonic expressions were concentrated around the Dongsha Island and within the study area that is situated far west only the thermal subsidence of the continental margin is existed (Xie et al., 2017; He et al., 2019; Wang et al., 2020; Lin et al., 2018a). Therefore, during the deposition of the study interval, we consider the tectonic background as overall stable and only the thermal subsidence played a role to create the accommodation space and accumulate the study succession.

2.2. Terrestrial sediment supply

The terrestrial sediments of the Pearl River margin are mainly from the Pearl River watershed (Fig. 1A). These tributaries have a main stem length of 2214 km, annual runoff of 3×10^{11} m³, a mean annual water discharge of 9600m³/s, and an annual suspended sediment discharge of 90 Mt. (Zhang et al., 2008; Wei and Wu, 2011). Because the catchment area would tend to be tectonically stable during a timescale of <1 My, the terrestrial sediment supply is assumed to be controlled mainly by the watershed climates. As the dominant component of the Asian climate system, Asia Monsoon, including East Asian Monsoon (EAM) and South Asian Monsoon (SAM), transports heat and moisture from the tropical west Pacific Ocean and south Indian Ocean across the equator and to higher latitudes (Wang et al., 2001; Mohtadi et al., 2016). It directly determines precipitation in the catchment, controls the strength of sediment yield and delivery (Zong et al., 2006), and thus, may have an influence on the development of deep-water systems at the terminal sink (Wan et al., 2007; Clift et al., 2014; Zhuo et al., 2015). Moreover, because EAM affects most area of the Pearl River catchment but SAM only influences the very-upper segment, the former is considered as the primary climatic driver for Pearl River source-to-sink sediment-routing system and its proxies is analyzed in detail in this study.

3. Datasets and methods

### 3.1. Seismic data to characterize sedimentary records

The 3D seismic survey used in this study covers the outer shelf and the slope segment of the Pearl River margin, with an area of 2000 km² and reaching down far onto an intraslope basin (Fig. 1B). It was acquired by China National Offshore Oil Corporation (CNOOC) and has a 4 ms vertical sampling rate and dominant frequency of 50 Hz in the study interval, yielding a vertical resolution of 7.5 m. Moreover, a regional 2D seismic line was also used in this study (Fig. 1A), which has a lower dominant frequency of 30 Hz in the interval of interest and results in an estimated vertical resolution of 12.5 m.

In this study, the seismic analysis for Pearl River deep-water sedimentary records is mainly conducted using the Paleoscan Software. The spectral decomposition Red-Green-Blue colour blends are generated from the 3D seismic volume and used to aid in seismic geomorphological-sedimentological analysis, which has significantly enhanced visualization of facies distribution and hence inference of depositional processes. On the other hand, to aid in calibration and interpretation, the planform geometry and amplitude or frequency variations on attribute maps are accompanied by cross-sectional seismic facies analysis. Seismic facies represent the different depositional elements of sedimentary records and they are recognized and defined mainly by the configurations of reflectors (reflection continuity and amplitude), cross-sectional geometries, and strata terminations.

3.2. Borehole data to characterize sedimentary records

Two shallow boreholes of ZQ3 and SH1B, acquired by Guangzhou Marine Geological Survey, were collected from the study area. ZQ3 is
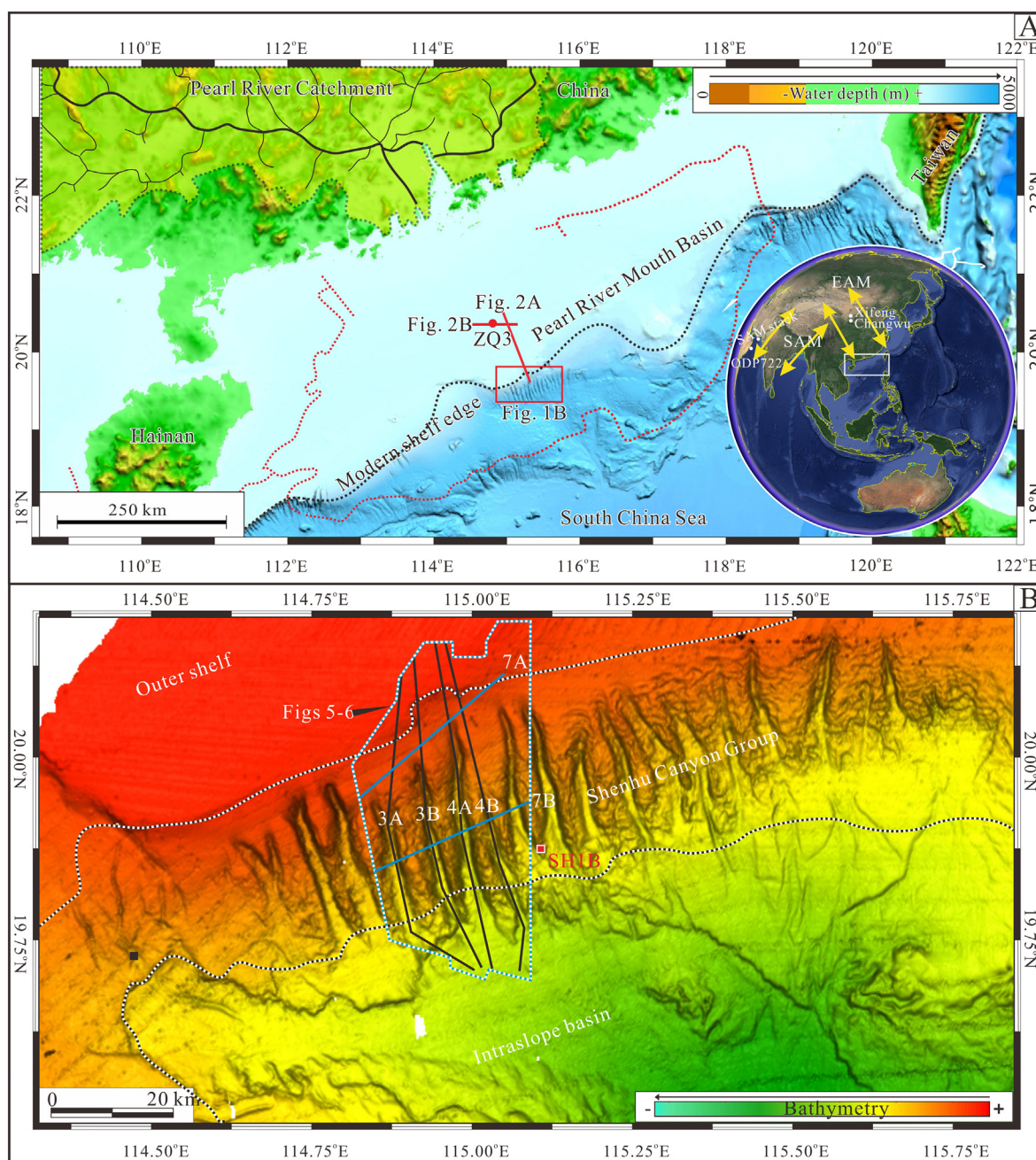
Fig. 1. (A) Physiography of the studied Pearl River sediment-routing system, from the catchment to the deep-water reach. The study area spans the shelf-edge and slope segments, as shown by the red rectangle (B). Also shown are the plan-view locations of the regional seismic lines shown in Fig. 2, and the well ZQ3 from Zhuo et al. (2015). (B) Bathymetric map of the present sea floor of the study area. The plan-view locations of seismic transects presented in Figs. 3, 4 (black solid lines), Fig. 7 (blue solid lines) and Fig. 8 (white solid lines), attribute maps shown in Figs. 5, 6, and borehole cores of SH1B are all shown. (For interpretation of the references to colour in this figure legend, the reader is referred to the web version of this article.)

located on the shelf segment of the Pearl River margin and the associated cores were analyzed by Feng et al. (1996). From ZQ3, Feng et al. (1996) collected samples for thermoluminescence (TL) dating and those TL ages have provided the basic chronological constraints for this study (Fig. 2). Based on these TL ages, several basinwide unconformities were dated through the seismic-well tie (Ludmann et al., 2001; Zhuo et al., 2015; Gong et al., 2018; Liu et al., 2019; Wang et al., 2020), which established the overall chronostratigraphic framework of the Quaternary Pearl River Margin.

Near the lateral boundary of a canyon mouth, core SH1B (ca. 1250 m water depth, 25 m long) was collected and analyzed in this study (Fig. 1B). Firstly, calcareous nannofossils assemblages were examined and described from smear slides made from core section samples.

According to the astronomical age estimates of calcareous nannofossil biohorizons of Ruffi et al. (2006), the recognized biostratigraphic events, mainly the first occurrence (FO) and last occurrence (LO) of diagnostic species, are tied to geologic timescale of Gradstein et al. (2012). Furthermore, the standard nannofossil zonations of Martini (1971) and Okada and Bukry (1980) were utilized to evaluate nannofossil age datums. Secondly, core SH1B was carefully sampled at an interval of 20 cm to examine the grain size and the contents of organic carbon (TOC) and calcium carbonate ($CaCO_3$). The grain-size analysis was conducted by a lase diffraction particle size analyzer (Mastersizer 2000) with a measurement range of 0.02-2000 um; before grain-size analysis, the gravel fraction was sieved, using sieves of 2000 um and 4000 um for collecting the gravel-grained particles. The content of TOC was measured using an
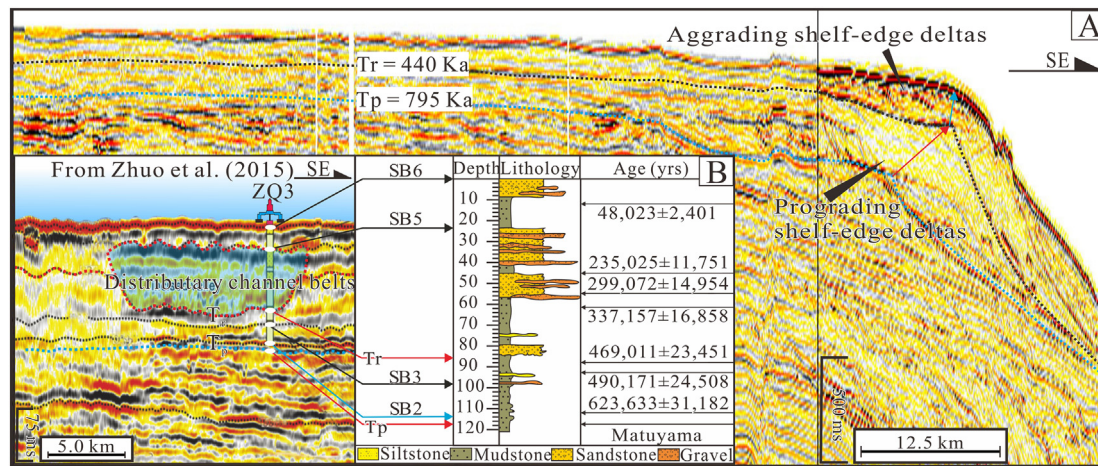
Fig. 2. (A) Regional 2D seismic transect that spans the shelf and slope segments and shows the stratigraphic architecture in the study area. Note that two regional unconformities (named T_p and T_r) have been clearly recognized. (B) Seismic-well tie transects illustrating the calibration between the T_p and T_r unconformities and thermoluminescence dates for ZQ3 (from Feng et al., 1996). Note that T_p and T_r are respectively constrained as the 795 Ka and 440 Ka, i.e. the dates of lowest sea level within MIS 20 and MIS 12.

organic element analyzer (EA1110); before the measurement, dry sediments were placed into the tin cup and then hydrochloric acid was added to remove the carbonate. The content of $CaCO_3$ was measured using the EDTA volumetric method. The sample was firstly dissolved and filtrated by the acetic acid and then the filtrate was adjusted to pH 13 by the potassium hydroxide; utilizing calcein as the indicator, we titrated the filtrate with EDTA standard solution until the disappearance of the green fluorescence. Lastly, SH1B cores are sampled at the interval of 10 cm to produce a $\delta^{18}O$ curve, which can be very helpful in establishing the age model of cores through correlating to global oxygen isotope records (Lisiecki and Raymo, 2005). Values of $\delta^{18}O$ were measured exclusively on the shells of planktonic foraminifera *Globigerinoides ruber*; the analysis were performed using MAT 253 mass spectrometer and then converted to PDB values.

In addition, in this study we applied the REDFIT algorithm (Schulz and Mudelsee, 2002), which has been widely used in cyclostratigraphic analysis of paleoclimatic data (Hodell et al., 2013; Cantalejo and Pickering, 2014; Husson et al., 2014), to conduct spectral estimation for above-mentioned stratigraphic-series. It can determine the statistically significant frequency of them so that we can quantitatively discriminate the sea-level signal within those sedimentary records.

3.3. Sea level curves and monsoon proxies

To reconstruct the fluctuations of sea levels and monsoonal climates in Quaternary, a series of previously published sea-level curves and monsoon proxies are considered in this study. Given the temporal resolution, continuity, and frequency of those published monsoonal signals, we decided to use the magnetic susceptibility of Chinese loess (Guo et al., 2009) as proxy of EAM intensity. It was measured in the Quaternary loess sections at Xifeng and Changwu in northern China (Fig. 1A); high values of magnetic susceptibility generally correlate to warm and wet climate, i.e. the intensified monsoon, whereas low values usually correspond to cool and dry climate, i.e. the relatively weak monsoon. For SAM, we selected the abundance of *G. bulloides* (a planktonic foraminifera commonly used as upwelling indicator) from ODP site 722 in Arabian Sea (Huang et al., 2007; Tripathi et al., 2017) to characterize the long-term variation of monsoonal intensity (Fig. 1A). Furthermore, to present the short-term variations of SAM, another multi-proxy Arabian Sea record (SAM stack) from Caley et al. (2011) is also presented in this study (Fig. 1A).

In addition, we choose the sea level curve of Miller et al. (2020) as the record of sea-level fluctuations in Pearl River margin. Miller et al.

(2020) reviewed many Phanerozoic sea-level changes and then presented a new and representative eustatic sea-level curve. Due to the tectonic stability of the study area as noted above and that the timescale of this study is <1 My, the amount of thermal subsidence is unlikely to have a significant impact on the sea level change (Blum et al., 2013; Romans et al., 2016). Therefore, Miller's global sea-level curve could be considered as representative of sea-level changes in Pearl River margin to some degree. Moreover, to obtain the variation law of eustasy and EAM, REDFIT spectral analysis for the curves of sea level and loess magnetic susceptibility were also performed.

4. Seismic stratigraphy and seismic facies

### 4.1. Unconformities and corresponding stratigraphic framework

4.1.1. Description of unconformities

Within the shelf and slope succession of the Quaternary Pearl River margin, there are two basinwide unconformities: T_p and T_r as shown in Figs. 3 and 4. They were recognized and named in our previous studies (Gong et al., 2018; Gong et al., 2019) and identified by some other works as well (SB2 and SB4 of Zhuo et al., 2015; SB2 and SB1 of Liu et al., 2019; H2 and H3 of Wang et al., 2020). Those two unconformities commonly show stratal toplap below and stratal downlap above in their proximal segments, but display onlap terminations in the distal reaches (Figs. 3 and 4). Furthermore, both T_p and T_r were tied to the shallow borehole ZQ3 through regional 2D seismic lines and the seismic-well tie points suggest T_p roughly correlates to the Matuyama paleomagnetic reversal boundary dated as 0.78 Ma, and that T_r is slightly younger than the TL age of 469,011 ± 23,451 yr B.P. (Fig. 2).

4.1.2. Interpretation of unconformities

Based on the above-mentioned correlation results and the assumption that basinwide unconformities represent significant periods of sea-level fall, we interpret the T_p and T_r unconformities to have formed during the most pronounced eustatic sea-level fall of Marine Isotope Stages 20 (MIS 20) and MIS 12. Those sea-level falls led to the regional regression and the subaerial exposure of the shelf and ultimately gave rise to the formation of T_p and T_r. According to Lisiecki and Raymo (2005), the lowest points of sea levels during MIS 20 and MIS 12 are respectively dated as 795 Ka and 440 Ka (Figs. 2B–4). Such chronological constraints are consistent with the works of Liu et al., 2019 and Wang et al., 2020, who also recognized and dated those two unconformities.
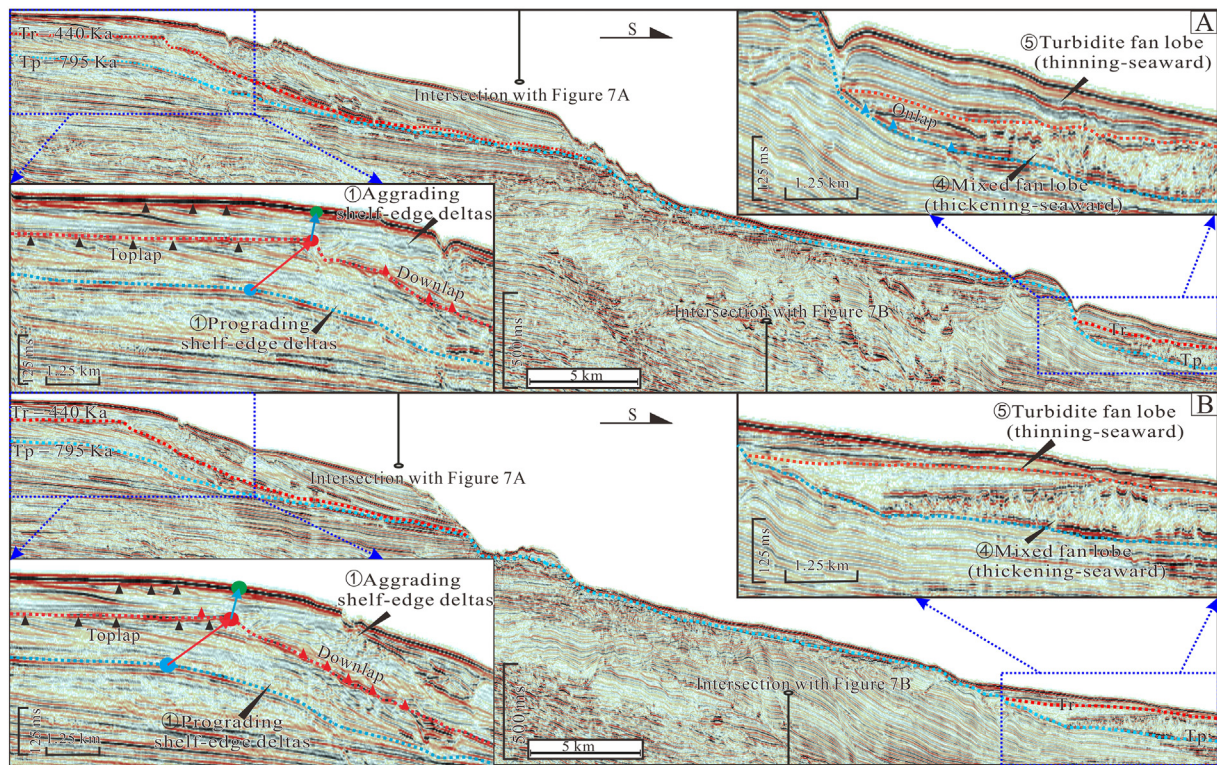
Fig. 3. Two dip-oriented seismic sections (A and B) with zoomed insets of shelf-edge and outlying deep-water segments (line locations shown in Fig. 1B) illustrating the stratigraphic architecture of the study area, where T_r and T_p are unconformities and respectively dated as 795 ka and 440 ka. Noted that in the proximal reaches, prograding shelf-edge deltas with slightly rising shelf-edge trajectories (red arrows) transformed to aggrading shelf-edge deltas with steeply rising shelf-edge trajectories (blue arrows). At the outlying deep-water reaches, mixed fan lobes that are thickening distally gave way to turbidite fan lobes that are gradually thinning. (For interpretation of the references to colour in this figure legend, the reader is referred to the web version of this article.)
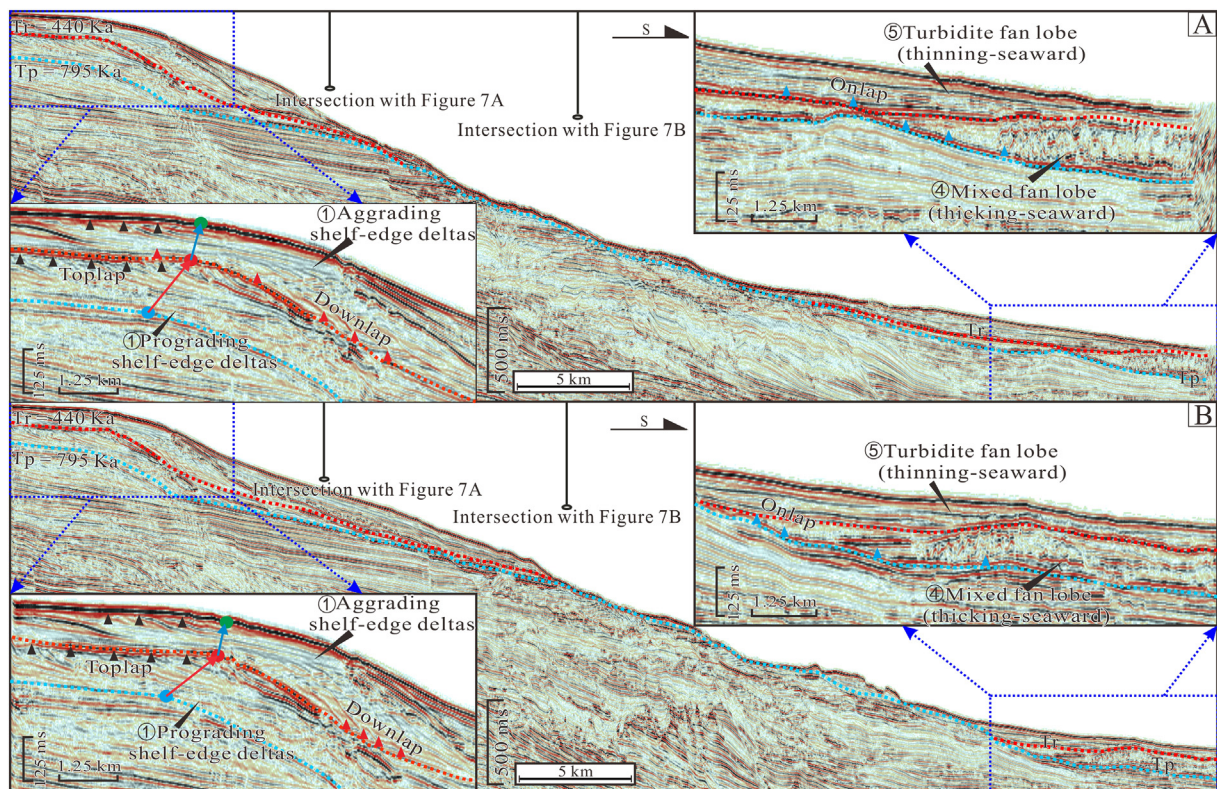
Fig. 4. Another two seismic sections along the depositional dip (A and B), which have reinforced the finds from Fig. 3: both of fan lobes and shelf-edge deltas have shown systematically variations. Line locations shown in Fig. 1B.

In this study, we consider the stratigraphic interval bounded by T_p and the present sea floor as the sedimentary record deposited over a longer timescale. Because the time interval (795 Ky) is near 1 My, we herein define that longer timescale as the 1 My-scale. On the other hand, the interval bounded by T_r and the present sea floor is the study succession containing multiple glacial-interglacial cycles, which are considered as the shorter timescale of this study. Due to those glacial-interglacial cycles in late Pleistocene correspond to a time interval of roughly 100 Ky, we herein define that shorter timescale as the 100 Ky-scale.

4.2. Seismic facies and corresponding depositional systems

4.2.1. Description of seismic facies

We totally define five dominant seismic facies based on the integration of cross-sections and seismic attribute maps (Table 1). Seismic facies 1 commonly occurs at the shelf-margin staging area. In cross sections, it is composed of sigmoid-oblique reflections that show toplap and erosional truncations upwards and downlap terminations at the base (Figs. 3 and 4, Table 1); in plain view, they are manifested as high-amplitude accumulations with a lobate shape downdip (Figs. 5, 6, Table 1). Seismic facies 2 collectively occur at the shelf edge and the upper slope, immediately downstream of the seismic facies 1. In cross sections, it is characterized by small V-shaped channel form with distinct basal surface (Fig. 7A; Table 1); in map view, it is expressed as low-sinuosity threads showing a tributary pattern (Figs. 5, 6, Table 1).

Seismic facies 3 shows distinct defining characteristics, such as cross-sectional V-shaped or U-shaped confinement and planform straight bands (Figs. 5–7B, Table 1). Occurring on the Pearl River slope, they do not incise the shelf edge but are characterized with eastwards migration along slope under the influence of bottom currents (Zhu et al., 2010; Gong et al., 2013; Gong et al., 2016b) (Figs. 5–7B). As for seismic facies 4 and seismic facies 5, they both occur in the intraslope basin (Figs. 1, 5 and 6); they accumulated at the mouth of seismic facies

3 and present fan or tongue shapes in map view (Figs. 5, 6, Table 1). However, in cross sections, these two facies show significant differences. Seismic facies 5 is completely composed of high-amplitude, continuous reflections; Seismic facies 4, however, shows additional chaotic and transparent reflections besides the continuous reflection packages (Figs. 3, 4, Table 1).
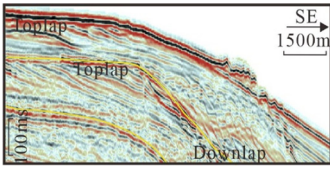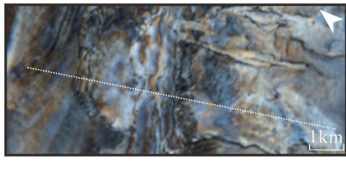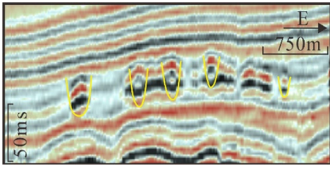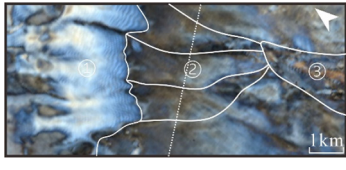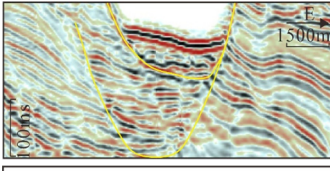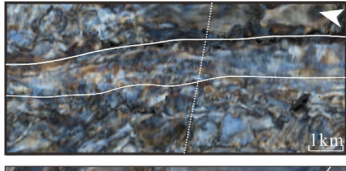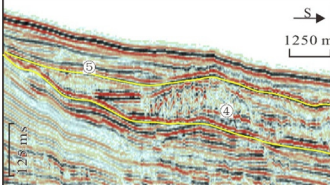
4.2.2. Interpretation of seismic facies

Because of the absence of well data and therefore of lithology information within the study area, the interpretation of seismic facies in terms of depositional elements is based on the comparison with published seismic-based studies on deep-water sedimentology. Firstly, seismic facies 1 in a shelf-edge position are commonly interpreted as shelf-edge deltas (Sylvester et al., 2012; Bourget et al., 2014); similar observations have also been made at the Pearl River margin by Lin et al. (2018b), Liu et al. (2019) and our previous studies (Gong et al., 2018; Gong et al., 2019). Secondly, seismic facies 2 showing a distinct tributary pattern immediately downdip of shelf-edge deltas is considered as tributary slope channels or gullies (Mulder et al., 1998; Posamentier and Kolla, 2003); in the offshore Ganges-Brahmaputra delta, similar seismic facies of deep-water tributary channels have also been documented by Rogers et al. (2015).

Lastly, in deep-marine environments, V- to U-shaped scours (i.e. seismic facies 3) and the splay deposits at their mouths (i.e. seismic facies 4 and 5) have been recognized globally as canyons (Deptuck et al., 2007; Hansen et al., 2017) and fan lobes (Posamentier and Kolla, 2003; Saller et al., 2008). Furthermore, because seismic facies 4 and 5 have apparently different reflection characteristics in cross sections, they are interpreted as different kinds of fan lobes. Facies 5 entirely composed of high-amplitude, continuous reflections are interpreted as traditional turbidite fan lobes. However, Facies 4 that have additional chaotic and transparent reflections are interpreted as mixed fan lobes, which refers to the depositional bodies that show evidence of both turbidites and mass-transport deposits (Gamberi and Rovere, 2011; Gamberi et al.,

Table 1

Tabulation of defined five kinds of seismic facies in the study interval as observed in cross sections and on attribute (spectral decomposition-RGB blend) maps.

| Seismic facies and interpretation	Reflection descriptions	Typical seismic cross-section	Typical RGB blend map
① Seismic facies 1: shelf-edge deltas (Sylvester et al., 2012; Bourget et al., 2014)	**Cross section**: Sigmoid-oblique reflections showing toplap and erosional truncations upward and downlap terminations at the base **Map view:** High-amplitude sheets with an apron shape downdip		
② Seismic facies 2: tributary channels (Mulder et al., 1998; Posamentier and Kolla, 2003)	**Cross section:** Small V-shaped channel form with distinct basal surface **Map view:** Low-sinuosity threads showing a tributary pattern and serving as the bridge between ① and ③		
③ Seismic facies 3: canyons (Deptuck et al., 2007; Hansen et al., 2017)	**Cross section:** U- to V-shaped deposits consisting of multiple stacked channel forms **Map view:** High-amplitude straight bands		
④ Seismic facies 4: mixed fan lobes; ⑤ Seismic facies 5: turbidite fan lobes (Gamberi and Rovere, 2011; Gamberi et al., 2014, 2015)	**Cross section:** Chaotic, transparent, and continuous reflections all show up in ④; high-amplitude and continuous reflections dominate ⑤ **Map view:** ④ and ⑤ both show fan-shaped, high-amplitude accumulations at the ends of ③		
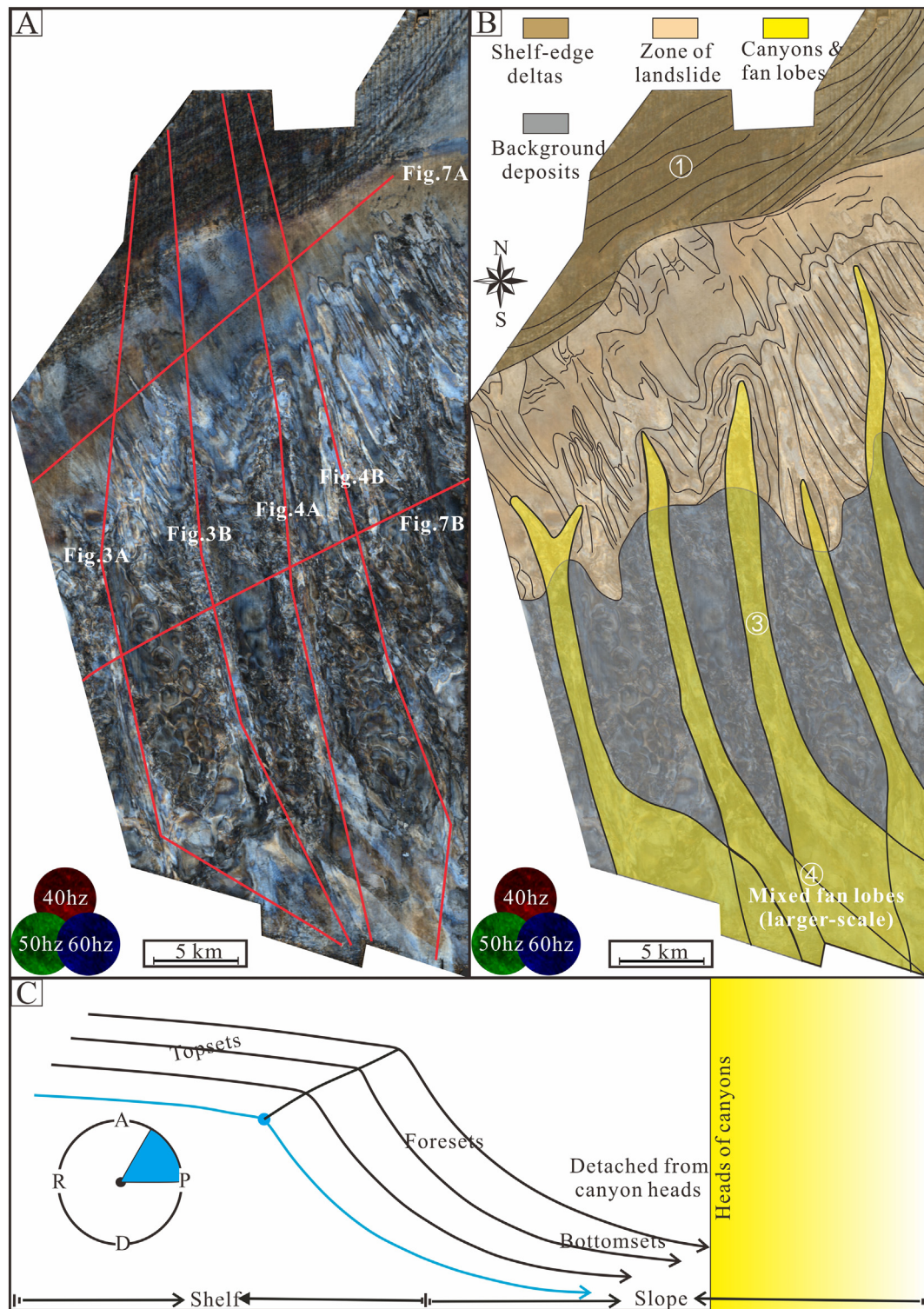
Fig. 5. (A–B) Representative spectral decomposition attribute map for the stratigraphic interval bounded by T$_p$ and T$_r$ and the associated interpretations. Noted that the mixed fan lobes at the outlying deep-water reaches have relatively larger scales compared with the counterparts occurred later, as shown in Fig. 6. Also, noted that for this stage of delta progradation, deltas around the shelf edge still kept a certain distance from the slope canyons and terrigenous sediments were mainly fed into canyons through the process of mass wasting. (C) Conceptual diagram of shelf-margin clinoforms associated with the accumulation of shelf-edge deltas from 795 ka to 440 ka. Noted that during this phase, shelf edges were slightly rising and that bottomsets of clinoforms were still detached from the heads of canyons. A = Aggradation; P = Progradation; D = Downward; R = Retrogradation.

2014, 2015). Canyons documented herein are the main conduits for the delivery of terrigenous sediments from the shelf to the deep water, and the fan lobes represent the accumulation area of gravity-flow deposits. Those depositional elements constitute the deep-water sedimentary system on the Pearl River margin, i.e. the focus of the present study.

5. Characterization of the deep-water sedimentary records

In this study, the characterization of the deep-water sedimentary record has been done in terms of two different timescales: the 1 My-scale and the 100 Ky-scale. Over the 1 My-scale, we mainly use the
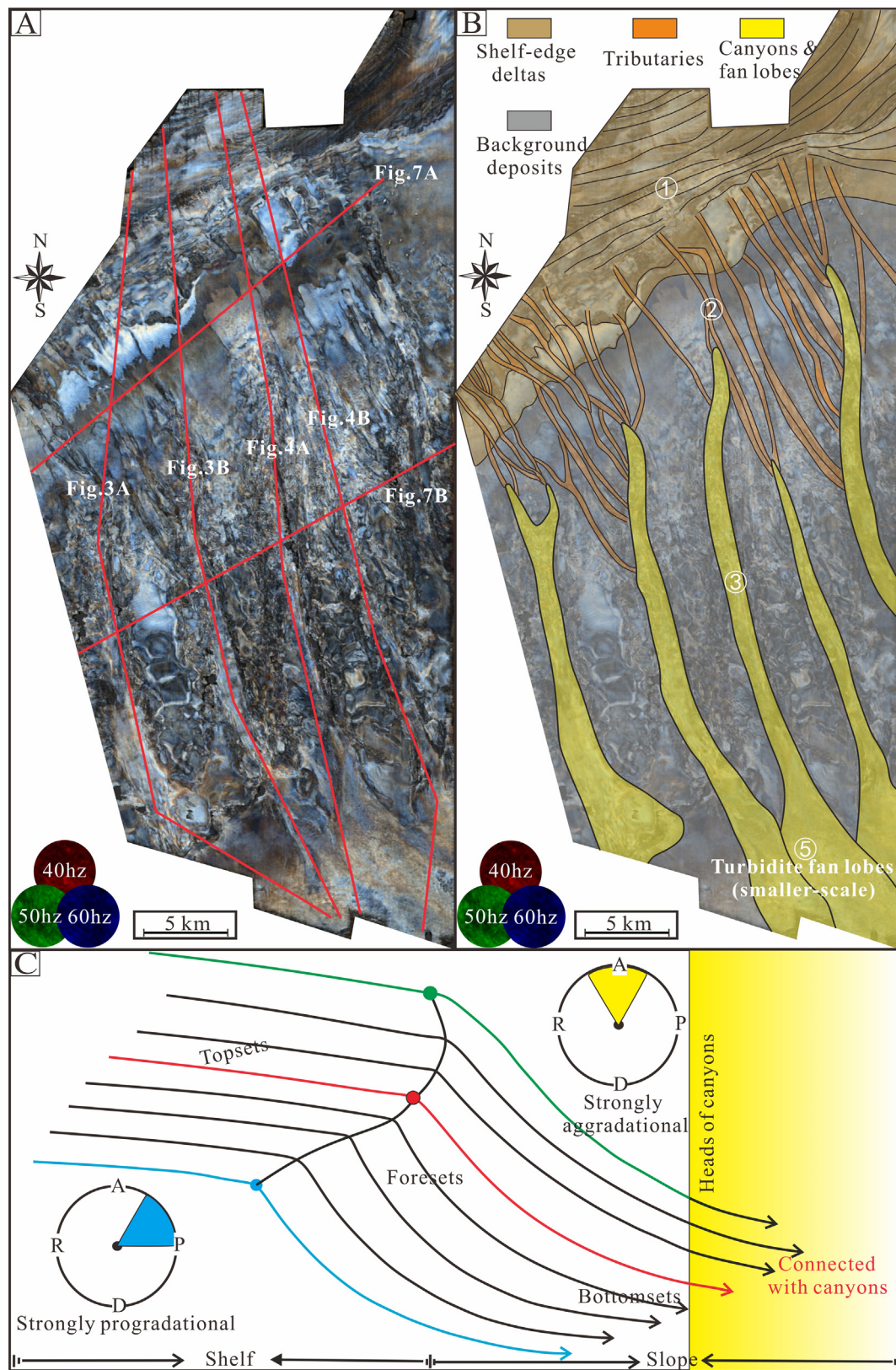
Fig. 6. (A–B) Representative spectral decomposition attribute map for the stratigraphic interval bounded by T$_r$ and the present seafloor and the associated interpretations. Turbidite fan lobes at that time are apparently smaller than those occurred early, as shown in Fig. 5. Noted that through the substantial progradation, deltas had connected with slope canyons through a series of tributary channels. (C) Conceptual diagram of shelf-margin clinoforms associated with the accumulation of shelf-edge deltas since 440 ka. Noted that shelf edges show steeply rising trajectories and that bottomsets of clinoforms were connected with canyons.
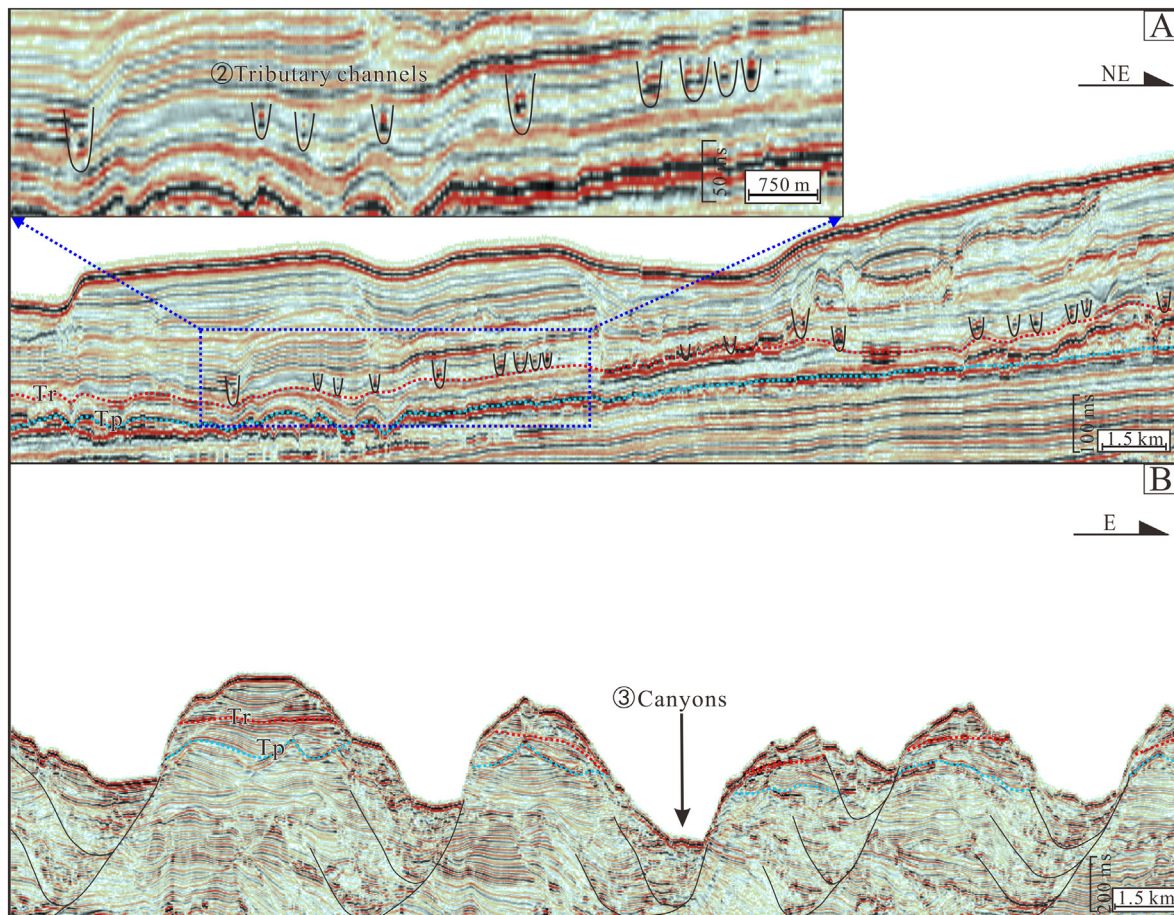
Fig. 7. (A) A strike-oriented seismic section with zoomed inset showing the details of cross-sectional expression of tributary channels (i.e. seismic facies 2) that are occurred immediately downstream of shelf-edge deltas. (B) Another strike-oriented seismic section along the slope segment showing the reflection characteristics of canyons (i.e. seismic facies 3).

seismic data to depict the change in architectural style of the deep-water system. However, in the case of the 100 Ky-scale theme, focus is on glacial-interglacial cycles since MIS 12, where borehole data are used to investigate the composition variations of deep-water deposits.

5.1. Architectural variations of the deep-water system at the 1 My-scale

In the stratigraphic interval bounded from T_p to the present sea floor, there are two discrete phases of stratigraphic record above and below horizon T_r, each of which has a given style of deep-water deposition (Figs. 3–6). Specifically, those two phases are an underlying series of mixed fan lobes (with large scale and more distal depocenters) and an overlying series of turbidite fan lobes (with smaller scales and more proximal depocenters) (Figs. 3–6).

5.1.1. Large mixed fan lobes and more distal depocenters

In the interval bounded by T_p and T_r, fan lobes in the outlying deep-water reaches show both chaotic, transparent, and continuous reflections in cross sections, matching the characteristics of seismic facies 4, i.e. mixed fan lobes (Figs. 3 and 4). Those mixed fan lobes are characterized by a gradually thickening trend in dip-oriented cross sections (Figs. 3, 4) and are spatially extensive in map view (Fig. 5), suggesting they have more distal depocenters and larger scales. Specifically, they have average thicknesses of 80-100 m and are 20-40 km in length, 20-30 km in width, 3-5 $\times$ 10^3 km^2 in area, and 2-5 $\times$ 10^5 km^3 in volume (Figs. 3–6). On the other hand, while mixed fan lobes developed in the distal deep water, shelf-edge deltas (Seismic facies 1) also occurred on the outer shelf segment of the Pearl River margin (Figs. 3–6). They were described in detail by our

previous studies (Gong et al., 2018; Gong et al., 2019) and interpreted as deltas with a progradation-dominated stacking pattern, corresponding to slightly rising shelf-edge trajectories (red arrows in Figs. 3 and 4).

5.1.2. Smaller turbidite fan lobes and more proximal depocenters

In the interval above T_r unconformity, sediment accumulation in the intraslope depocenter exhibit high-amplitude and continuous reflections and thus, are interpreted as turbidite fan lobes (Seismic facies 5) (Figs. 3, 4). Those turbidite fan lobes show gradually thinning trends in cross sections (Figs. 3, 4) and have relatively limited extension areas in plain view (Fig. 6), suggesting they have more proximal depocenters and smaller scales. Specifically, they are only 20-40 m in thickness, 15-30 km in fan length, 10-20 km in fan width, 1-3 $\times$ 10^3 km^2 in area, and 2–10 $\times$ 10^4 km^3 in volume (Figs. 3–6). Also, those turbidite fan lobes are linked to coeval shelf-edge deltas, which are strongly aggradational and correspond with steeply rising shelf-edge trajectories (blue arrows in Figs. 3 and 4) (Gong et al., 2018; Gong et al., 2019).

5.2. Composition variations of deep-water deposits at the 100 Ky-scale

At the 100 Ky-scale, i.e. within the glacial-interglacial cycles, marine-core analysis from borehole SH1B suggests that there are significant differences in composition between glacial and interglacial deposits (Figs. 8–10).

5.2.1. Age model of sediment cores

Borehole SH1B is near the lateral boundary of a canyon mouth, immediately out of the 3D seismic survey (Fig. 1B). Although it is not viable
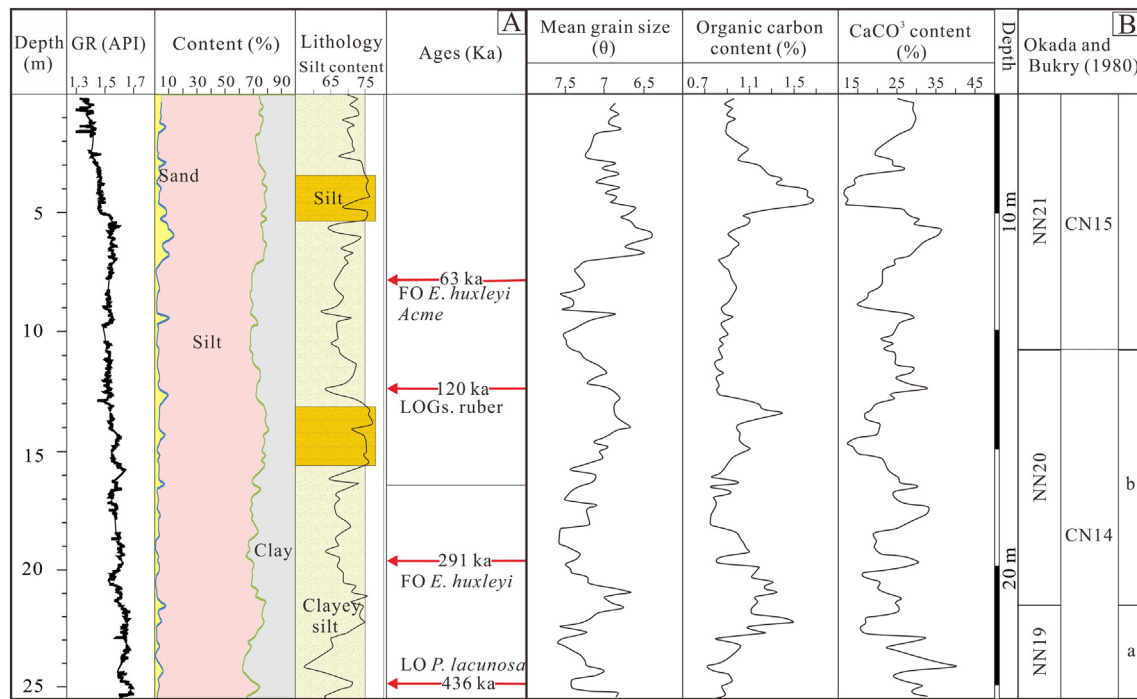
Fig. 8. (A) SH1B stratigraphic column showing the Gamma Ray curve, sediment contents, lithological characteristics, and the occurrences of biostratigraphic events. (B) Several stratigraphic-series of core SH1B, including the mean grain size and the contents of organic carbon (TOC) and calcium carbonate (CaCO³).

to conduct a detailed seismic-well tie, the abovementioned seismic characterization for the deep-water system strongly indicates that the SH1B cores are dominated by fan-lobe sediments bypassed through the upslope canyon. Furthermore, because the core is near the lateral boundary of the canyon mouth and is at a certain distance from the main axis of the fan lobes, it has a stable depositional setting, corresponds to generally fine grain sizes, probably low sedimentation rates, and thus likely reflects a relatively large time window.

To exam variations of deep-water system accumulation within the 100 Ky-scale of glacial-interglacial cycles, we need to establish an age model of core SH1B. Firstly, through a careful study of calcareous nannofossil biostratigraphy, four biostratigraphic events, named *LOP. lacunose, FOE. huxleyi, LOGs. ruber, and FOE. huxleyiAcme* from oldest to youngest age, are recognized, and they are respectively dated as 436 Ka, 291 Ka, 120 Ka and 63 Ka according to the astronomical age estimates of calcareous nannofossil biohorizons of Ruffi et al. (2006) (Fig. 8). Then, taking these four biostratigraphic-event chronologies as the reference, we tuned the δ18O time series of core SH1B to the oxygen isotope records of Lisiecki and Raymo (2005) using QAnalySeries Software (Kotov and Pälike, 2018). As shown in Fig. 9 and Table 2, four biostratigraphic-event ages vary little through that tuning procedure, which means the chronological correlation is well within the biostratigraphic dating error. Finally, we plotted the tuned δ18O *G. ruber* pointers that represent the start and end dates of several recent glacial periods, i.e. the boundaries between blue and white bars in Fig. 9C, on the depth scale of core SH1B to establish a high-resolution age model. As shown in Table 3, the chronostratigraphic framework of SH1B since MIS 12 includes five main glacial-interglacial cycles and was well developed down to 25.05 m.

5.2.2. Composition variations through the sediment cores in glacial-interglacial cycles

To investigate the variations in the composition of fan deposits, SH1B cores were carefully sampled to measure the lithofacies, grain-sizes, and the content of organic carbon (TOC) and calcium carbonate (CaCO₃), all of which present cyclic variations (Fig. 8). Based on the established age model (Fig. 9; Table 3), we can put these data into the glacial-interglacial cycles to exam their detailed variations (Fig. 10).

Though SH1B cores are dominated by a silt component (Fig. 8), there are slight variations from the bottom to the top and thus, the lithological facies could be further divided into silt (with silt contents >75 %) and clayey silt (with silt contents <75 %) (Fig. 8). According to the age model, two layers of silt recognized at borehole depths of 530-340 cm and 1564–1310 cm (Fig. 8) occur respectively in time intervals of 31–15 Ka and 178–138 Ka, both of which represent the glacial-maximum phase of glacial periods, i.e. the Last Glacial Period (LGP) and the Penultimate Glacial Period (PGP) (Fig. 10). Moreover, the mean grain sizes of samples were also calculated after the method of Folk and Ward (1957) to produce a continuous mean grain size curve (Fig. 8). As shown in Fig. 10, when putting that grain size curve into the context of age model, its temporal evolution is clearly shown: coarser-grained sediments, with relatively smaller θ values, occurred in the glacial periods (grey bars in Fig. 10) whereas finer-grained deposits, with relatively larger θ values, correspond to the interglacial periods (white bars in Fig. 10). In addition, apart from the lithological and grain-size characteristics, SH1B cores also show significant variations in chemical constituents. As shown in Fig. 10, TOC and CaCO₃ curves respectively have similar and opposite variation trends with respect to the curve of mean grain size. Compared with sediments deposited in interglacial periods, glacial coarser-grained deposits have relatively larger TOC contents and relatively smaller CaCO₃ fractions.

6. Sea-level control on the development of the deep-water system

As stated above, deep-water sedimentary records within both the 1 My-scale and the 100 Ky-scale have shown systematic variations. We then related those variations to the contemporaneous eustatic sea-level changes to investigate the coupling relationships between them.

6.1. Sea-level fluctuation causes time change in the overall architecture of the deep-water system at the 1 My-scale

As stated above, at the 1 My-scale, the studied deep-water system shows clearly a transitional change in overall architecture at 440 Ka: mixed fan lobes with larger scales and more distal depocenters gave
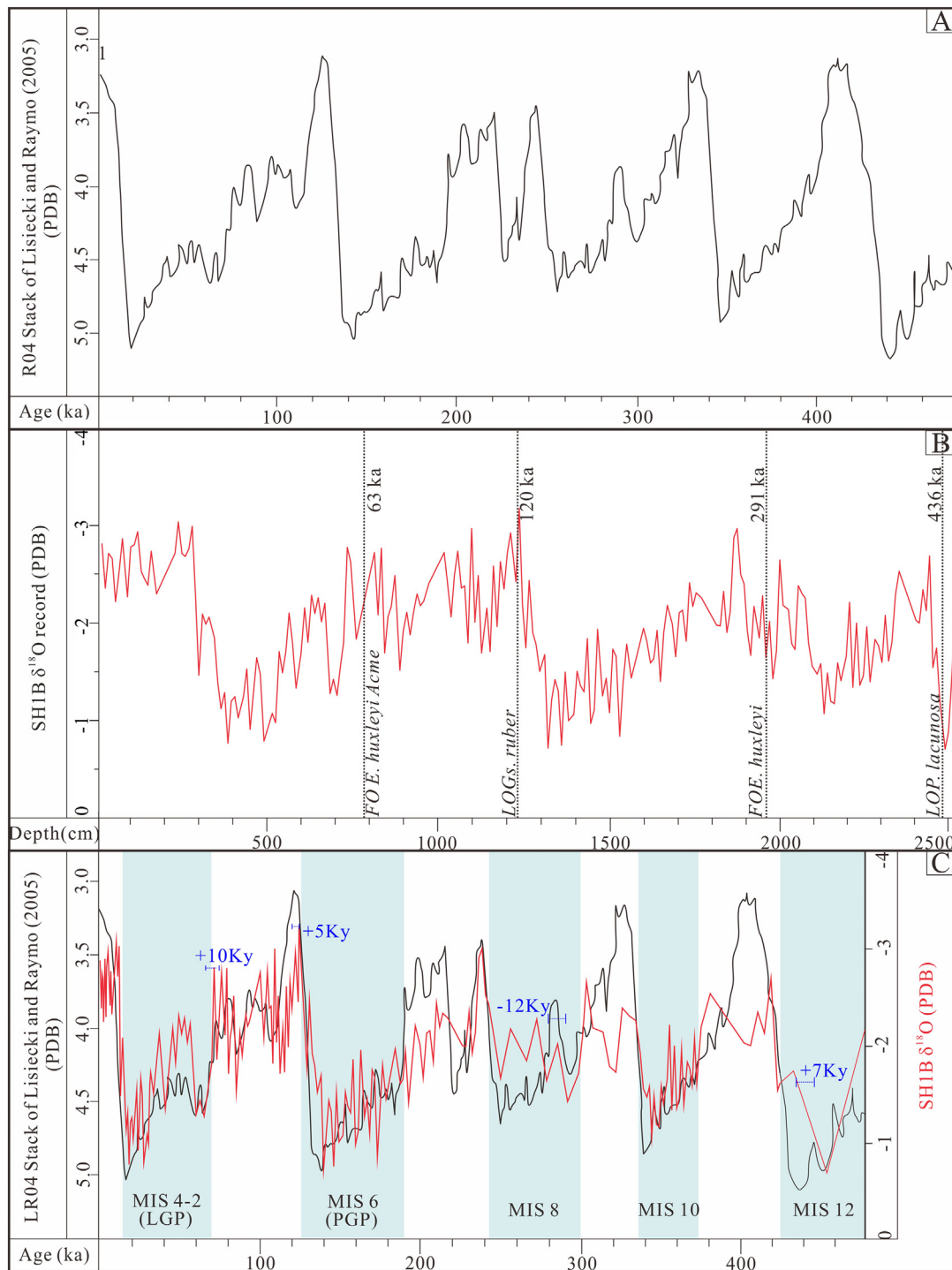
Fig. 9. (A) The oxygen isotope records of Lisiecki and Raymo (2005) since the start date of MIS 12. (B) The oxygen isotope records of SH1B cores on the depth scale. (C) The result of tuning SH1B δ18O records (the red line) to the oxygen isotope records of Lisiecki and Raymo (2005) using QAnalySeries Software (the black line). Noted that through the tuning process, all four biostratigraphic-event ages only have slight changes, where positive values are times when tuned ages are more than the biostratigraphic ages and negative values are times when the tuned ages are less than the biostratigraphic ages. (For interpretation of the references to colour in this figure legend, the reader is referred to the web version of this article.)

way to turbidite fan lobes with smaller scales and more proximal depocenters. If sea-level forcings caused this change in architecture, perhaps the most convincing test would be a demonstration that the changes of sea-level behavior occurred concurrently with the depositional variation. We therefore analyzed the fluctuation characteristics of the sea level during the time interval of 795–440 Ka and 440 Ka-present. The results suggest that during 795–440 Ka mean level was −70.3 m with a relatively smaller standard deviation of ±23.9 m, suggesting low-amplitude sea-level fluctuations (Fig. 11). By contrast, after 440 Ka

mean level was −59.9 m, with a relatively larger standard deviation of ±35.0 m, suggesting high-amplitude sea level changes (Fig. 11). In addition, REDFIT spectrum analysis for the sea level curve indicates that the dominant frequency of sea-level oscillations also changed, from 42 Ky in 795-440 Ka to 100 Ky in 440 Ka-present, i.e. from obliquity cycles to short-eccentricity cycles (Fig. 11). As shown in Fig. 11B, sea level oscillations within those two intervals are respectively well correlated with obliquity and eccentricity curves calculated by Berger (1978). This abrupt variation in sea-level fluctuation characteristics
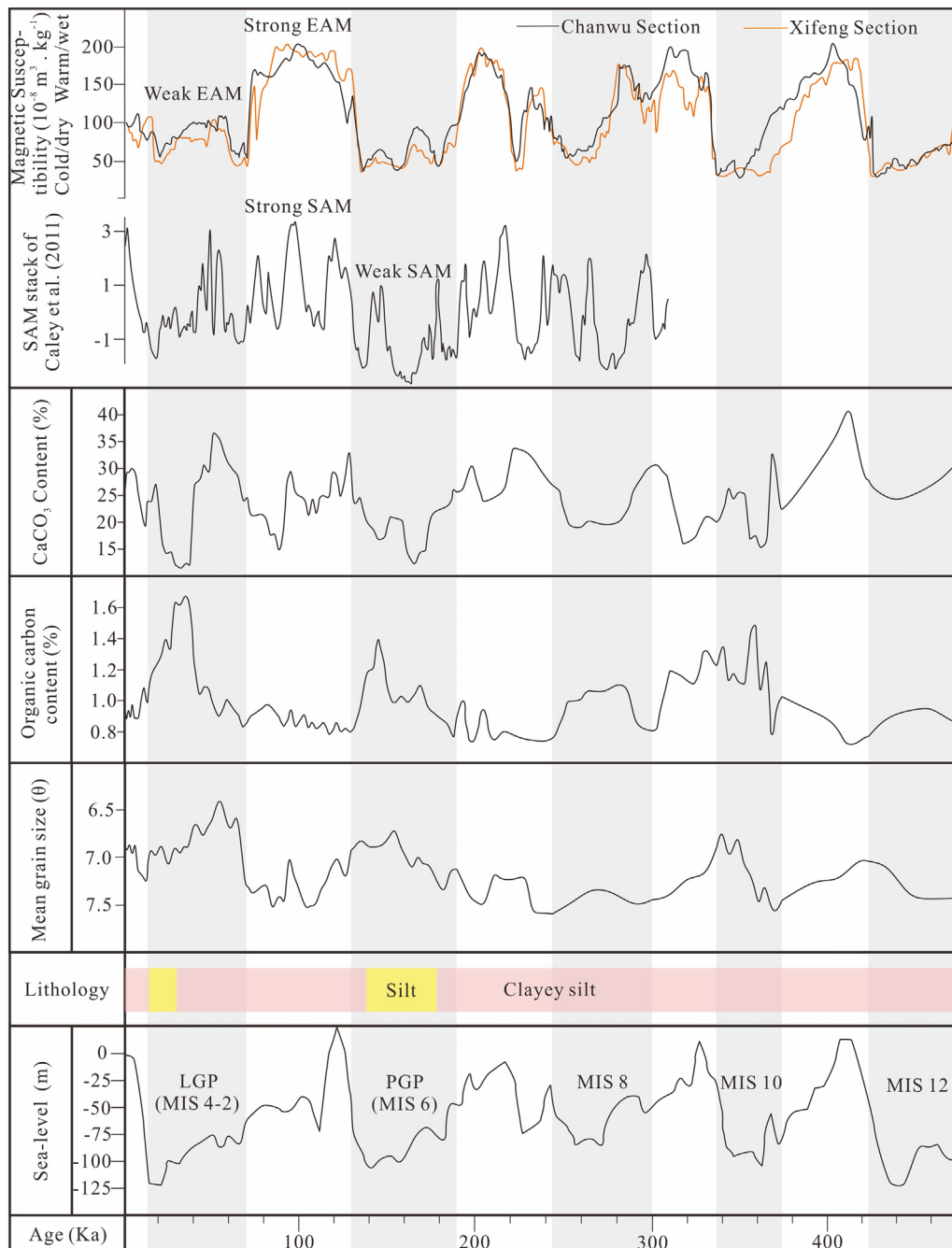
Fig. 10. Temporal evolution of the composition characteristics of SH1B cores in comparison with sea-level curve and the monsoon fluctuations (including EAM proxied by the magnetic susceptibility of Chinese loess and SAM proxied by the Arabian Sea stacked records). Noted that the composition characteristics of fan sediments vary in line with orbital forced fluctuations in sea level. The sea level curve, the loess magnetic susceptibility, and the SAM stack are respectively referred from Miller et al. (2020), Guo et al. (2009), and Caley et al. (2011).

seems to be related to the occurrence of Mid-Brunhes Event (MBE), recognized as evidence of a climatic change in a number of marine sediments and Antarctic ice cores and characterized by a further increase

Table 2
SH1B biostratigraphic-event chronologies and the adjusted results when tuning the $\delta^{18}O$ time series of core SH1B to the oxygen isotope records of Lisiecki and Raymo (2005) using QAnalySeries Software (Kotov and Pälike, 2018).

Depths (cm)	Biostratigraphic events	Ages (Ka)	Tuned ages (Ka)	Error (Ky)
790	FOE. huxleyiAcme	63	73	+10
1230	LOGs. ruber	120	125	+5
1960	FOE. huxleyi	291	279	−12
2490	LOP. lacunosa	436	443	+7

of ice-volume variations with, from then to the present day, four large-amplitude 100-Kyr-dominated glacial-interglacial cycles (EPICA community members, 2004) (Fig. 11B).

Above all, it is concluded that 795–440 Ka and 440 Ka-present are two independent intervals, between which the overall architecture of the deep-water system and the fluctuations characteristics of sea levels are significantly different. More specifically, mixed fan lobes with larger scales and more distal depocenters in the older phase are seen to be contemporaneous with low-amplitude and high-frequency sea-level fluctuations, whereas turbidite fan lobes with smaller scales and more proximal depocenters in the younger phase are shown to be coeval with high-amplitude and low-frequency sea-level oscillations (Fig. 11). Therefore, it is reasonable to believe that the amplitude and

Table 3

Results of plotting tuned δ¹⁸O *G. ruber* pointers that represent the start and end dates of several most recent glacial periods on the depth scale of core SH1B. LGP = Last Glacial Period; PGP = Penultimate Glacial Period; MIS = Marine Isotope Stage.

Glacial sea-level lowstand	LGP (MIS 4-MIS 2)	PGP (MIS 6)	MIS 8	MIS 10	MIS 12
Time interval (ka)	70-14	191-130	300-243	374-337	478-424
SH1B core interval (cm)	715-285	1630-1253	1996-1897	2337-2085	2505-2445

frequency characteristics of eustatic sea level have controlled the overall architecture of the deep-water system.

Within 795–440 Ka time interval, low-amplitude and high-frequency sea-level fluctuations, on one hand would allow the shoreline to prograde rapidly across the shelf; on the other hand, it would also have caused the delta to reside more frequently in a position close to the shelf edge, thereby enhancing the progradation of shelf edge deltas and the sediment transfer to deep water (Porębski and Steel, 2003; Sømme et al., 2009; Zhang et al., 2017). Therefore, during this older phase, shelf-edge deltas have slightly rising trajectories, and outlying fan lobes have relatively larger scales and more distal depocenters (Fig. 11). That coupling relationship between fan lobes and shelf-edge trajectories is consistent with the studies of Carvajal et al. (2009) and Gong et al. (2015), who argued that rates of shelf-edge progradation are roughly proportional to the total volumes of sediments partitioned into deep-water setting. However, it must be noted that for most of the time of that older phase, the sea-level-forced progradation of shelf edge deltas was not enough to achieve their connection with downslope canyons. The canyon feeding at that time, therefore, may be dominated by delta-front failures, as shown by the representative seismic geomorphology for the lower stratigraphic interval (Fig. 5). As a result, those fan lobes with larger scales and more distal depocenters tend to be deposited from mass-wasting flows and their transformed turbidity flows, resulting in complex facies consisting of both mass-transport deposits and turbidites.

Within 440 Ka-present, high-amplitude and low-frequency fluctuations of eustatic sea levels served to decrease the efficiency of shoreline regression across the shelf and reduce the proportion of time that the deltas were able to stay close enough to the shelf edge, thereby disfavoring the sediment partitioning to deep water (Porębski and Steel, 2003; Sømme et al., 2009; Zhang et al., 2017). Consequently, during this younger phase, shelf deltas stored more of the sediment budget on the shelf, and strongly aggraded, in turn bypassing meagre sediment volumes to the slope, causing fan lobes to have relatively smaller scales and more proximal depocenters (Fig. 11). In addition, due to the continuous progradation of shelf-edge deltas, they were able to overreach the shelf break far enough at that time and attached with the heads of slope canyons through a series of tributary channels, as shown in Fig. 6. These tributary channels acted as a bridge between deltas and canyons, within which sediment bypassing was one of the mechanisms of sediment transport from widely separated river mouths to canyon heads. Therefore, the canyon feeding during this younger phase may be dominated by river-born sediments. As a result, the fan lobes with smaller scales and more proximal depocenters tended to originate from pure turbidity flows, giving rise to the formation of turbidite fan lobes.

6.2. Sea-level stands determined the sediment composition of the deep-water system at the 100 Ky-scale

Over the 100 Ky-scale, i.e. within the glacial-interglacial cycles, our data suggest there are significant compositional differences between deep-water sediments that were deposited in glacial and interglacial periods respectively. Coarser-grained deposits, with higher TOC content and lower CaCO₃ content and sometimes expressed as silts, occurred preferentially in the glacial periods, i.e. during the sea level lowstands (Fig. 10). However, finer-grained sediments having lower OC and higher CaCO₃ contents and expressed as clayey silts were deposited in the interglacial periods, i.e. the sea-level highstands (Fig. 10). Therefore, it clear that periodic changes of sea-level stands driven by Milankovitch

(short-eccentricity) cycles have controlled the composition of the deep-water system.

To further validate sea-level control on the composition of sediments, we conducted REDFIT spectrum analysis for the stratigraphic-series of deep-water deposits. The results suggest a spectrum of curves for oxygen isotope, grain-size, OC content, and CaCO₃ content. All have three main significant frequencies above the 90 % confidence level (Fig. 12A–D) among which the first one is dominant, just like the spectrums of contemporaneous curves of sea levels (Fig. 11A) and loess magnetic susceptibility (Fig. 12E). Statistically, these three significant frequencies are respectively positioned at 0.156–0.182, 0.479–0.603, 0.877–1.045 cycles/m (Table 4). To convert these frequencies to temporal durations, a reliable average sedimentation rate for the whole core SH1B is needed. Thus, we establish an age-depth curve based on the start and end dates of last five glacial periods (Table 3) and the linear fitting formula gives a value of average sediment accumulation rate of 4.72 cm/Ky (Fig. 12F). Applying the 4.72 cm/Ky to estimate the REDFIT significant frequencies suggests the presence of 116–135 Ky, 35–44 Ky, and 20–24 Ky temporal periods (Table 4), which are very close to the significant frequencies of sea-level series (i.e. 100 Ky, 40 Ky and 24 Ky shown in Fig. 11A) and corresponding to the orbital parameters of eccentricity, obliquity, and precession respectively (Table 4). To conclude, stratigraphic-series of deep-water deposits and the time series of sea levels all faithfully respond to Milankovitch climatic forcings and have very similar spectrum characteristics, further validating the tight coupling relationship between the compositions of deep-water deposits and the stands of sea levels.

During interglacial sea-level highstands, the high sea levels result in anomalously large shelf accommodation, long shoreline transit times, and sediment entrapment on the inner shelf (Burgess and Hovius, 1998; Muto and Steel, 2002). Thus, interglacial terrigenous sediments are relatively hard to be partitioned into deep water, giving rise to finer-grained sediments. However, during glacial sea-level lowstands, regression of shorelines brought the Pearl River mouth to the outer-shelf or shelf-margin staging area, promoting the delivery of terrigenous sediments to deep water; in the meantime, the profound exposure of the shelf caused the early deposits to be eroded and reworked offshore, reinforcing the terrigenous sediment supply (Liu et al., 2010, 2016; Zhao et al., 2017). As a result, during sea-level lowstands, terrigenous sediments are much more easily delivered into deep water, forming relatively coarser sediments. Moreover, these explanations of increased terrigenous input during glacial sea-level lowstands versus decreased sediment input within interglacial sea-level highstands are consistent with the variations of chemical constituents of deep-water sediments. For example, during glacial sea-level lowstands, the strong terrigenous input brings abundant nutrients for biological activity, which result in a bloom of marine primary productivity and thus enhance the contents of organic carbon (Fig. 10) (Ning et al., 2004; Zhao et al., 2017; Peng et al., 2021). On the contrary, such increased terrigenous inputs tend to dilute the deep-sea carbonate, thus producing relatively low content of calcium carbonate (Fig. 10) (Scotchman et al., 2015; Zhao et al., 2017).

*6.3. Further discussion about the role of eustatic sea level in driving the growth of deep-water systems*

Strictly speaking, the growth of deep-water systems can be governed by numerous forcing factors, autogenic (sea-floor topographic, avulsions
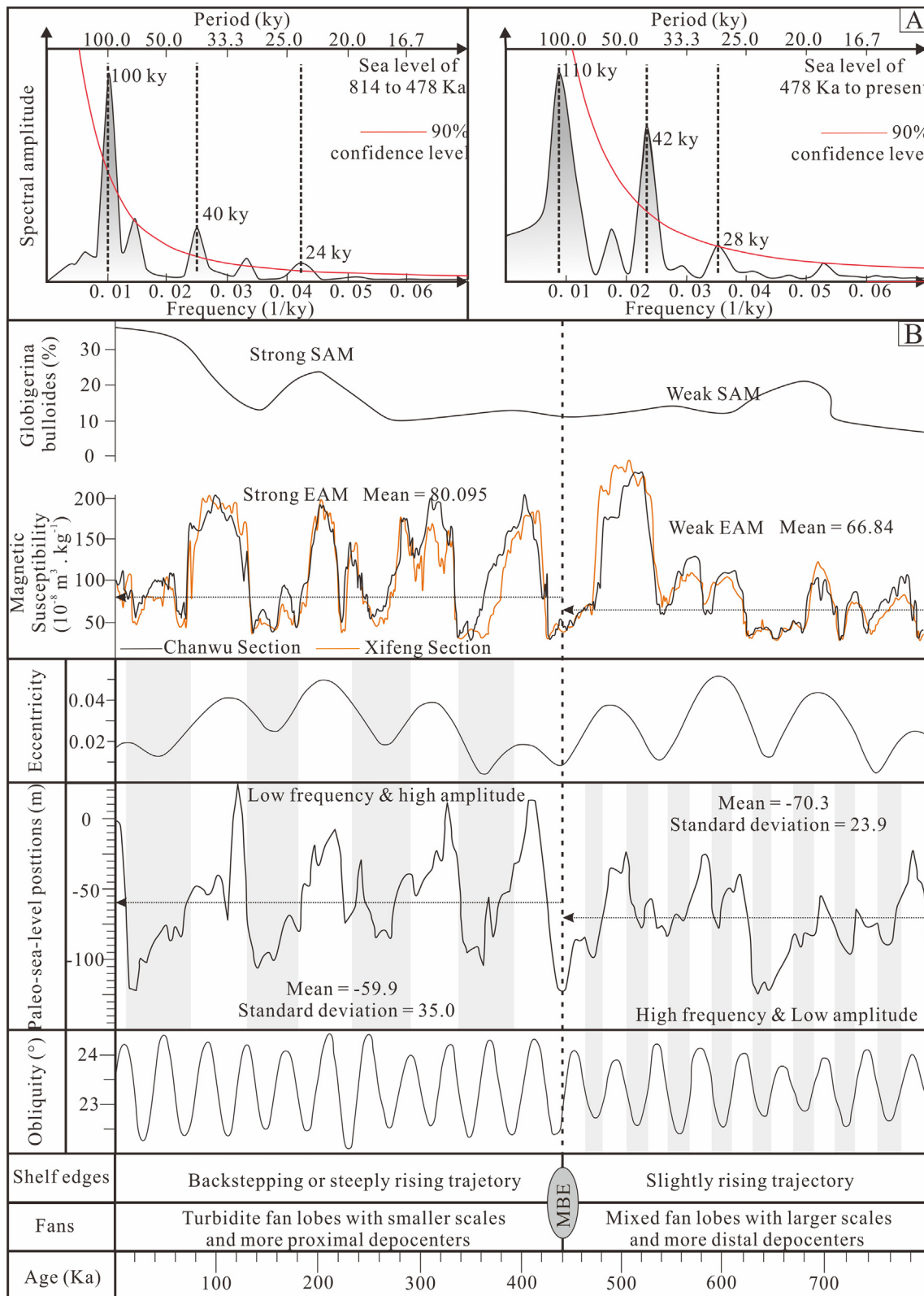
Fig. 11. (A) Results of REDFIT spectrum analysis for the sea level curve of Miller et al. (2020) during the time interval of 795 to 440 Ka (left panel) and 440 Ka to present (right panel). (B) Temporal evolution of the overall architecture of deep-water sedimentary records in comparison with the sea-level curve (Miller et al., 2020) and the strength of EAM proxied by the magnetic susceptibility of Chinese loess (Guo et al., 2009) and of SAM proxied by the abundance of *Globigerina bulloides* from ODP site 722 in Arabian Sea (Huang et al., 2007; Tripathi et al., 2017). In addition, the correlation between the sea-level curve and orbital parameters (Berger, 1978) is also performed; sea-level fluctuations during 795-440 Ka are well correlated with obliquity cycles, whereas oscillations since 440 Ka are matched with the eccentricity cycles. MBE = Mid-Brunhes Event.
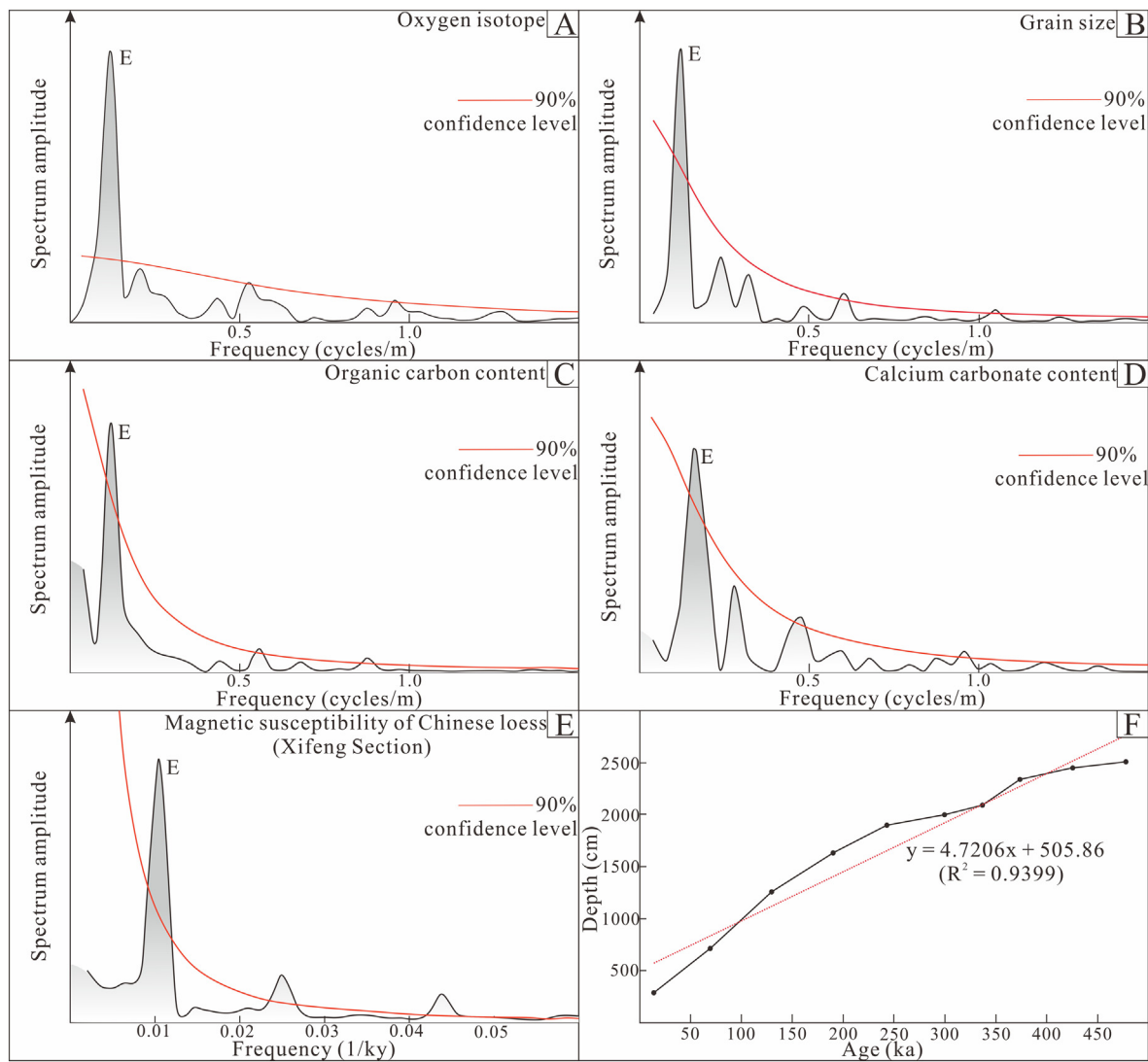
Fig. 12. (A–E) REDFIT spectrum determined from each SH1B stratigraphic-series and the time series of loess magnetic susceptibility. (F) An age-depth curve of the SH1B cores (solid line) and the associated linear regression trendline (dashed line). The "time nodes" represent the start and end dates of last five glacial periods (Table 3) and the linear fitting formula gives a value of average sediment accumulation rate of 4.72 cm/ky. In each REDFIT spectrum result, three significant frequencies are identified above the 90 % confidence level and using the average sediment accumulation rate of 4.72 cm/ky, the temporal duration of each frequency can be estimated, as shown in Table 4. Furthermore, frequencies corresponding to orbital eccentricity (E) time periods are labelled.

of channels, dynamic of current) and allogenic (tectonic, eustasy, terrigenous sediment supply). However, on the Quaternary Pearl River margin, eustatic sea-level forcings did play the first-order control, which is because the obscuration of other forcing factors can be ruled out to some

Table 4
Spectrum results and temporal duration estimate for the stratigraphic-series of borehole SH1B.

Stratigraphic-series	Significant frequencies (cycles/m)	Temporal period (kyr)	Orbital parameters
Oxygen isotope	0.158	134.1	Eccentricity
	0.519	40.8	Obliquity
	0.957	22.1	Precession
Grain size	0.161	131.6	Eccentricity
	0.603	35.1	Obliquity
	1.045	20.3	Precession
Organic carbon content	0.156	135.8	Eccentricity
	0.558	38.0	Obliquity
	0.877	24.2	Precession
GaCO3 content	0.182	116.4	Eccentricity
	0.479	44.2	Obliquity
	0.957	22.1	Precession

degree. Firstly, given the fact that our studied deep-water system consists of stable canyons and associated fan lobes, it is unlikely that autogenic process caused significant changes in sediment dispersal. Therefore, autogenic factors would not have great influence on the overall evolution of the deep-water system. Secondly, for tectonic forcings, both of tectonic activities and thermal subsidence can play a role on the development of deep-water systems. On the Quaternary northern South China Sea margin, because the only neotectonic activity (Dongsha tectonism) is concentrated on the Dongsha Island, our study area is considered as tectonically stable (Xie et al., 2017; He et al., 2019; Wang et al., 2020). There is very low possibility of having large-scale sediment gravity flows triggered by earthquakes related to tectonic activities. Furthermore, within a timescale of <1 My, the amount of thermal subsidence tends to be limited (Blum et al., 2013; Romans et al., 2016), which minimize its impact on the growth of deep-water systems. Therefore, tectonic controls are not discussed further in this study and we suggest that only monsoon-controlled sediment supply may have important impacts on the development of the deep-water system on the Pearl River margin.

However, that speculation on monsoonal climates is not consistent with the correlation results between the observed sedimentary records and the strength of EAM and SAM. Within both the shorter and longer

timescales, relatively strong EAM (proxied by high loess magnetic susceptibility) and SAM (proxied by high Arabian stack records and high abundance of *Globigerina bulloides* from ODP site 722) that occurred in interglacial periods (Fig. 10) and the time interval of 440 Ka-present (Fig. 11B) respectively correspond to deep-water sediments with surprisingly fine grain sizes and fan lobes with small scales and proximal depocenters. In other words, high sediment discharges caused by heavy precipitation during warm and wet (strong) monsoon climates did not produce efficient sediment delivery to deep-water areas, nor did it cause significant growth of the deep-water system. Therefore, it is strongly suggested that the monsoonal climates in drainage basins did not play a dominant role in the development of the deep-water system. On the contrary, sea level forcings was likely the first-order control. Such argument is also consistent with previous studies (Feng et al., 1996; Liu et al., 2010; Zhuo et al., 2015; Liu et al., 2016), all of which highlight due to the shelf characteristics of great width (>200 km) and gentle gradient (0.03°–0.05°), sedimentation in the Pearl River shelf and the outlying deep-water area is very sensitive to sea-level fluctuations.

In addition, through the correlation between sedimentary records and sea-level behaviors, we find that sea-level forcings have played varied roles in driving the growth of the deep-water system at the 1 My-scale and the 100 Ky-scale. This may be associated with the duration of the shoreline being close to the shelf edge. According to traditional sequence stratigraphy, sea-level forcing of sediment delivery relies on regression of shorelines to bring terrestrial sediments to the shelf-margin staging area and then to deep water. Over a relatively short time period, even though the shoreline system is close to the shelf edge at a given time, it will tend to recede back to the inner shelf with the subsequent rise of sea level, especially for late Quaternary when only 10 % of the cycle duration is occupied by maximum lowstand phase during the glacial acme (Lobo and Ridente, 2014). That short residence time is unfavorable for stable sediment export from river mouths or the profound remobilization of shelf-margin sediments. Therefore, glacial sea-level lowstand periods are less efficient in driving the terrigenous sediments into deep water though they do drive the composition variation of deep-water deposits. However, over a relatively long timescale, even though high-frequency sea level fluctuations still cause repeated cross-shelf transits of the shoreline, there is nevertheless long-enough cumulative time when the shoreline system is close to the shelf edge. This totally longer residence time at the shelf edge can guarantee sediment being stably fed into deep water. Thus, the change in sea-level fluctuation characteristics within the 1 My-scale manage to exert great influence on the terrigenous inputs and ultimately impact the overall architecture of the deep-water system.

7. Conclusions

(1) Within both the 1 My-scale and the 100 Ky-scale, the changing character of deep-water sedimentary records on the Quaternary Pearl River margin is related to the eustatic sea-level changes, which acted as the first-order control on the development of the deep-water system.

(2) During the 1 My-scale, the facies, size, and depocenters of the deep-water system all showed significant changes through time. Mixed fan lobes with larger scales and more distal depocenters correlate to low-amplitude and high-frequency sea-level fluctuations. However, turbidite fan lobes with smaller scales and more proximal depocenters correspond to high-amplitude and low-frequency sea-level fluctuations. Such correlations suggest that at even the 1 My-scale, it was mainly sea level that controlled the overall architecture of the deep-water system.

(3) At the 100 Ky-scale, the composition of deep-water deposits was significantly different between glacial sea-level lowstands and interglacial sea-level highstands. Coarse-grained deposits

with higher organic carbon contents and lower calcium carbonate contents characteristically deposited during glacial sea-level lowstands, while finer-grained deposits with lower organic carbon contents and higher calcium carbonate contents corresponded to the interglacial sea-level highstands. Thus, also at 100 Ky-scale, sea-level stands exerted an influence and controlled the sediment composition of the deep-water system.

Data availability statement

The data used for the research described in this article are sensitive without an open-source online data repository. Please contact the corresponding author for the detailed information.

Declaration of competing interest

We declare that we have no financial and personal relationships with other people or organizations that can inappropriately influence our work.

Acknowledgements

References

Berger, A., 1978. Long-term variations of caloric insolation resulting from the Earth's orbital elements. Quaternary Research 9, 139–167.

Blum, M.D., Martin, J., Milliken, K., Garvin, M., 2013. Paleovalley systems: insights from Quaternary analogs and experiments. Earth-Science Reviews 116, 128–169.

Bourget, J., Ainsworth, R.B., Thompson, S., 2014. Seismic stratigraphy and geomorphology of a tide or wave dominated shelf-edge delta (NW Australia): processbased classification from 3D seismic attributes and implications for the prediction of deep-water sand. Marine and Petroleum Geology 57, 359–384.

Burgess, P.M., Hovius, N., 1998. Rates of delta progradation during highstands: consequences for timing of deposition in deep-marine systems. Journal of the Geological Society 155, 217–222.

Caley, T., Malaize, B., Zaragosi, S., Rossignol, L., Bourget, J., Eynaud, F., Martinez, P., Giraudeau, J., Charlier, K., Ellouz-Zimmermann, N., 2011. New Arabian Sea records help decipher orbital timing of Indo-Asian monsoon. Earth and Planetary Science Letters 308, 433–444.

Cantalejo, B., Pickering, K.T., 2014. Climate forcing of fine-grained deep-marine systems in an active tectonic setting: Middle Eocene, Ainsa Basin, Spanish Pyrenees. Palaeogeography, Palaeoclimatology, Palaeoclimatology 410, 351–371.

Carvajal, C.R., Steel, R.J., 2006. Thick turbidite successions from supply-dominated shelves during sea-level highstand. Geology 34, 665–668.

Carvajal, C., Steel, R.J., Petter, A., 2009. Sediment supply: the main driver of shelf-margin growth. Earth-Science Reviews 96, 221–248.

Castelltort, S., Honegger, L., Adatte, T., Clark, J.D., 2017. Detecting eustatic and tectonic signals with carbon isotopes in deep-marine strata, Eocene Ainsa Basin, Spanish Pyrenees. Geology 45, 15–18.

Catuneanu, O., 2020. Sequence stratigraphy of deep-water system. Marine and Petroleum Geology 114, 104238.

Clift, P.D., Hodges, K.V., Heslop, D., Hannigan, R., Van Long, H., Calves, G., 2008. Correlation of Himalayan exhumation rates and Asian monsoon intensity. Nature Geoscience 1, 875–880.

Clift, P.D., Wan, S., Blusztajn, J., 2014. Reconstructing chemical weathering, physical erosion and monsoon intensity since 25 Ma in the northern South China Sea: a review of competing proxies. Earth-Science Reviews 130, 86–102.

Covault, J.A., Graham, S.A., 2010. Submarine fans at all sea-level stands: tectono-morphologic and climatic controls on terrigenous sediment delivery to the deep sea. Geology 38, 939–942.

Covault, J.A., Romans, B.W., Fildani, A., McGann, M., Graham, S.A., 2010. Rapid climatic signal propagation from source to sink in a southern California sediment-routing system. The Journal of Geology 118, 247–259.

Covault, J.A., Kostic, S., Paull, C.K., Sylvester, Z., Fildani, A., 2017. Cyclic steps and related supercritical bedforms: building blocks of deep-water depositional systems, western North America. Marine Geology 393, 4–20.

Deptuck, M.E., Sylvester, Z., Pirmez, C., O'Byrne, C., 2007. Migration–aggradation history and 3-D seismic geomorphology of submarine channels in the Pleistocene Beninmajor Canyon, western Niger Delta slope. Marine and Petroleum Geology 24, 406–433.

Ding, W., Li, J., Li, J., Fang, Y., Tang, Y., 2013. Morphotectonics and evolutionary controls on the Pearl River canyon system, south China sea. Marine Geophysical Research 34, 221–238.

EPICA community members, 2004. Eight glacial cycles from Antarctic ice core. Nature 429, 623–628.

Fauquembergue, K., Fournier, L., Zaragosi, S., Bassinot, F., Kissel, C., Malaiz, B., Caley, T., Moreno, E., Bachelery, P., 2019. Factors controlling frequency of turbidites in the Bengal fan during the last 248 kyr cal BP: clues from a presently inactive channel. Marine Geology 415, 1–13.

Feng, Z., Feng, W., Xue, W., Liu, Z., Chen, J., Li, W., 1996. Evaluation of Marine Geologic Hazards and Engineering Geological Conditions in the Northern South China Sea. Hehai University Publishing House, Nanjing, China, p. 178 (In Chinese).

Folk, R.L., Ward, W.C., 1957. Brazos River Bar: a study in the significance of grain size parameters. Journal of Sedimentary Research 27, 3–26.

Franke, D., Barckhausen, U., Baristeas, N., Engels, M., Ladage, S., Lutz, R., Montano, J., Pellejera, N., Ramos, E.G., Schnabel, M., 2011. The continent ocean transition at the southeastern margin of the South China Sea. Marine and Petroleum Geology 28, 1187–1204.

Galloway, W.E., 1989. Genetic stratigraphic sequences in basin analysis. II. Application to northwest Gulf of Mexico Cenozoic Basin. American Association of Petroleum Geologists Bulletin 73, 143–154.

Gamberi, F., Rovere, M., 2011. Architecture of a modern transient slope fan (Villafranca fan, Gioia basin-Southeastern Tyrrhenian Sea). Sedimentary Geology 236, 211–225.

Gamberi, F., Rovere, M., Mercorella, A., Leidi, E., 2014. The influence of a lateral slope on turbidite lobe development on a modern deep-sea slope fan (Villafranca deep-sea fan, Tyrrhenian Sea). Journal of Sedimentary Research 84, 475–486.

Gamberi, F., Rovere, M., Marani, M.P., Dykstra, M., 2015. Modern submarine canyon feeder-system and deep-sea fan growth in a tectonically active margin (northern Sicily). Geosphere 11, 307–319.

Gong, C., Wang, Y., Zhu, W., Li, W., Xu, Q., 2013. Upper Miocene to Quaternary unidirectionally migrating deep-water channels in the Pearl River Mouth Basin, northern South China Sea. American Association of Petroleum Geologists Bulletin 97, 285–308.

Gong, C., Wang, Y., Steel, R., Olariu, C., Xu, Q., Liu, X., Zhao, Q., 2015. Growth styles of shelf-margin clinoforms: prediction of sand- and sediment-volume partitioning into and across the shelf. Journal of Sedimentary Research 85, 209–229.

Gong, C., Steel, R.J., Wang, Y., Lin, C., Olariu, C., 2016a. Shelf-margin architecture variability and its role in source-to-sink sediment budget partitioning. Earth-Science Reviews 154, 72–101.

Gong, C., Wang, Y., Steel, R.J., Peakall, J., Zhao, X., Sun, Q., 2016b. Flow processes and sedimentation in unidirectionally migrating deep-water channels: from a 3D seismic perspective. Sedimentology 63, 645–661.

Gong, C., Blum, M.D., Wang, Y., Lin, C., Xu, Q., 2018. Can climatic signals be discerned in a deep-water sink?: an answer from the Pearl River source-to-sink sediment-routing system. Geological Society Association Bulletin 130, 661–677.

Gong, C., Steel, R.J., Wang, Y., Sweet, M.L., Xian, B., Xu, Q., Zhang, B., 2019. Shelf-edge delta overreach at the shelf break can guarantee the delivery of terrestrial sediments to deep water at all sea-level stands. American Association of Petroleum Geologists Bulletin 103, 65–90.

Gradstein, F.M., Ogg, J.G., Schmitz, M.D., Ogg, G.M., 2012. The Geological Time Scale 2012. Elsevier, Amsterdam.

Guo, Z., Berger, A., Yin, Q.Z., Qin, L., 2009. Strong asymmetry of hemispheric climates during MIS-13 inferred from correlating China loess and Antarctica ice records. Climate of the Past 5, 21–31.

Hansen, L., Janocko, M., Kane, I., Kneller, B., 2017. Submarine channel evolution, terrace development, and preservation of intra-channel thin-bedded turbidites: Mahin and Avon Channels, Offshore Nigeria. Marine Geology 383, 146–167.

He, M., Zhu, W., Wu, Z., Zhong, G., Ren, J., Liu, L., Wang, W., 2019. Neotectonic movement characteristics and hydrocarbon accumulation of the Pearl River Mouth basin. China Offshore Oil Gas 31, 9–20.

Hodell, H., Crowhurst, S., Skinner, L., Tzedakis, P.C., Margari, V., Channell, J.E.T., Kamenov, G., Maclachlan, S., Rothwell, G., 2013. Response of Iberian Margin sediments to orbital and suborbital forcing over the past 420 ka. Paleoceanography 28, 185–199.

Huang, Y., Clemens, S., Liu, W., Wang, Y., Prell, W., 2007. Large-scale hydrological change drove the late Miocene C4 plant expansion in the Himalayan foreland and Arabian Peninsula. Geology 6, 531–534.

Husson, D., Thibault, N., Galbrun, B., Gardin, S., Minoletti, F., Sageman, B., Huret, E., 2014. Lower Maastrichtian cyclostratigraphy of the Bidart section (Basque country, SW France): a remarkable record of precessional forcing. Palaeogeography, Palaeoclimatology, Palaeoecology 395, 176–197.

Jiwarungrueangkul, T., Liu, Z., Zhao, J., 2019. Terrigenous sediment input responding to sea level change and East Asian monsoon evolution since the last deglaciation in the southern South China Sea. Global and Planetary Change 174, 127–137.

Jorry, S.J., Jegou, I., Emmanuel, L., Silva Jacinto, R., Savoye, B., 2011. Turbiditic levee deposition in response to climate changes: the Var Sedimentary Ridge (Ligurian Sea). Marine Geology 279, 148–161.

Khripounoff, A., Vangriesheim, A., Crassous, P., Etoubleau, J., 2009. High frequency of sediment gravity flow events in the Var submarine canyon (Mediterranean Sea). Marine Geology 263, 1–6.

Kotov, S., Pälike, H., 2018. QAnalySeries – A Cross-Platform Time Series Tuning and Analysis Tool. AGU.

Li, S.T., Lin, C.S., Zhang, Q.M., Yang, S.G., Wu, P.K., 1999. Episodic rifting dynamics of the continental marginal basins and tectonic events since 10 Ma IN THE South China Sea. China Science Bulletin 44, 9–22.

Li, J., Liu, S., Shi, X., Zhang, H., Fang, X., Cao, P., Yang, G., Xue, X., Khokiattiwong, S., Kornkanitnan, N., 2019. Sedimentary responses to the sea level and Indian summer monsoon changes in the central Bay of Bengal since 40 ka. Marine Geology 415, 105947.

Lin, C., Jiang, J., Shi, H., Zhang, Z., Liu, J., Qin, C., Li, H., Ran, H., Wei, A., Tian, H., Xing, Z., Yao, Q., 2018a. Sequence architecture and depositional evolution of the northern continental slope of the South China Sea: responses to tectonic processes and changes in sea level. Basin Research 30, 568–595.

Lin, C., He, M., Steel, R., Zhang, Z., Li, H., Zhang, B., Wu, W., Shu, L., Tian, H., Zhang, X., Xing, Z., Wang, S., Zhang, M., 2018b. Changes in inner- to outer-shelf delta architecture, Oligocene to Quaternary Pearl River shelf-margin prism, northern South China Sea. Marine Geology 404, 187–204.

Lisiecki, L.E., Raymo, M.E., 2005. A Pliocene–Pleistocene stack of 57 globally distributed benthic δ18O records. Paleoceanography 20, PA1003.

Liu, Z., Colin, C., Ge, H., 2010. A high-resolution clay mineralogical record in the northern South China Sea since the Last Glacial Maximum, and its time series provenance analysis. Chinese Science Bulletin 55, 4058–4068.

Liu, X., Rendle-Buhring, R., Henrich, R., 2016. Climate and sea-level controls on turbidity current activity on the Tanzanian upper slope during the last deglaciation and the Holocen. Quaternary Science Reviews 133, 15–27.

Liu, H., Lin, C., Zhang, Z., Zhang, B., Jiang, J., Tian, H., Liu, H., 2019. High-resolution sequence architecture and depositional evolution of the Quaternary in the northeastern shelf margin of the South China Sea. Acta Oceanologica Sinica-English Edition 38, 86–98.

Lobo, F., Ridente, D., 2014. Stratigraphic architecture and spatio-temporal variability of high-frequency (Milankovitch) depositional cycles on modern continental margins: an overview. Marine Geology 352, 215–247.

Lopez, M., 2001. Architecture and depositional pattern of the Quaternary deep-sea fan of the Amazon. Marine and Petroleum Geology 18, 479–486.

Ludmann, T., Wong, H.K., Wang, P.X., 2001. Plio-Quaternary sedimentation processes and neotectonics of the northern continental margin of the South China Sea. Marine Geology 172, 331–358.

Martini, E., 1971. Standard Tertiary and Quaternary calcareous nannoplankton zonation. In: Farinacci, A. (Ed.), Proceedings of the Second Planktonic Conference, Roma 1970. vol. 2. Edizioni Tecnoscienza, Rome, pp. 739–785.

Mayall, M., Jones, E., Casey, M., 2006. Turbidite channel reservoirs-key elements in facies prediction and effective development. Marine and Petroleum Geology 23, 821–841.

Miller, K.G., Browning, J.V., Schmelz, W.J., Kopp, R.E., Mountain, G.S., Wright, J.D., 2020. Cenozoic sea-level and cryospheric evolution from deep-sea geochemical and continental margin records. Science Advances 6, eaaz1346.

Mitchum, R.M., 1985. Seismic stratigraphy expression of submarine fans. In: Berg, O.R., Wolverton, G.D. (Eds.), Seismic Stratigraphy. American Association of Petroleum Geologist Bulletinvol. 39, pp. 117–138.

Mohtadi, M., Prange, M., Steinke, S., 2016. L Palaeoclimatic insights into forcing and response of monsoon rainfall. Nature 533, 191–199.

Mulder, T., Savoye, B., Piper, D.J.W., Syvitski, J.P.M., 1998. The Var submarine sedimentary system: understanding Holocene sediment delivery processes and their importance to the geological record. Journal of the Geological Society 129, 145–166.

Muto, T., Steel, R.J., 2002. In defense of shelf-edge delta development during falling stage and lowstand. Journal of Geology 110, 421–436.

Ning, X., Chai, F., Xue, H., Cai, Y., Liu, C., Shi, J., 2004. Physical-biological oceanographic coupling influencing phytoplankton and primary production in the South China Sea. Journal of Geophysical Research 109, C10005.

Normark, W.R., Piper, D.J.W., Romans, B.W., Covault, J.A., Dartnell, P., Sliter, R.W., 2009. Submarine canyon and fan systems of the California continental borderland. In: Lee, H.J., Normark, W.R. (Eds.), Earth Science in the Urban Ocean: The Southern California Continental Borderland. vol. 454. Geological Society of America Special Paper, Boulder, Colorado, pp. 141–168.

Okada, H., Bukry, D., 1980. Supplementary modification and introduction of code numbers to the low-latitude coccolith biostratigraphic zonation (Bukry, 1973; 1975). Marine Micropaleontology 5, 321–325.

Peng, J.W., 2021. Sedimentology of the Upper Pennsylvanian organic-rich Cline Shale, Midland Basin: from gravity flows to pelagic suspension fallout. Sedimentology 68, 805–833.

Peng, J.W., Fu, Q.L., Larson, T.E., Janson, X., 2021. Trace-elemental and petrographic constraints on the severity of hydrographic restriction in the silled Midland Basin during the late Paleozoic ice age. Geological Society of America Bulletin 133, 57–73.

Picot, M., Droz, L., Marsset, T., Dennielou, B., Bez, M., 2016. Controls on turbidite sedimentation: insights from a quantitative approach of submarine channel and lobe architecture (Late Quaternary Congo fan). Marine and Petroleum Geology 72, 423–446.

Picot, M., Marsset, T., Droz, L., Dennielou, B., Baudidn, F., Hermoso, M., Rafelis, M., Sionneau, T., Cremer, M., Laurent, D., Bez, M., 2019. Monsoon control on channel avulsions in the Late Quaternary Congo Fan. Quaternary Science Reviews 204, 149–171.

Piper, D.J.W., Normark, W.R., 2009. Processes that initiate turbidity currents and their influence on turbidites; a marine geology perspective. Journal of Sedimentary Research 79, 347–362.

Porębski, S.J., Steel, R.J., 2003. Shelf-margin deltas: their stratigraphic significance and relation to deepwater sands. Earth-Science Reviews 62, 283–326.

Porębski, S.J., Steel, R.J., 2006. Deltas and sea-level change. Journal of Sedimentary Research 76, 390–403.

Posamentier, H.W., Kolla, V., 2003. Seismic geomorphology and stratigraphy of depositional elements in deep-water settings. Journal of Sedimentary Research 73, 367–388.

Posamentier, H.W., Allen, P.G., James, P.D., Tesson, M., 1992. Forced regression in a sequence stratigraphic framework: concepts, examples, and exploration significance. American Association of Petroleum Geologists Bulletin 76, 1687–1709.

Rogers, K.G., Goodbred, S.L., Khan, S.R., 2015. Shelf-to-canyon connections: Transport-related morphology and mass balance at the shallow-headed, rapidly aggrading Swatch of No Ground (Bay of Bengal). Marine Geology 369, 288–299.

Romans, B.W., Normark, W.R., McGann, M.M., Covault, J.A., Graham, S.A., 2009. Coarse-grained sediment delivery and distribution in the Holocene Santa Monica Basin, California: implications for evaluating source-to-sink flux at millennial time scales. Geological Society of American Bulletin 121, 1394–1408.

Romans, B.W., Castelltort, S., Covault, J.A., Fildani, A., Walsh, J.P., 2016. Environmental signal propagation in sedimentary systems across timescales. Earth-Science Reviews 153, 7–29.

Ru, K., Pigott, J.D., 1986. Episodic rifting and subsidence in the South China Sea. American Association of Petroleum Geologists Bulletin 70, 1136–1155.

Ruffi, I., Backman, J., Fornaciari, E., Palike, H., Rio, D., Lourens, L., Hilgen, F., 2006. A review of calcareous nannofossil astrobiochronology encompassing the past 25 million years. Quaternary Science Reviews 25, 3113–3137.

Saller, A., Werner, K., Sugiaman, F., Cebastiant, A., May, R., Glenn, D., Barker, C., 2008. Characteristics of Pleistocene deep-water fan lobes and their application to an upper Miocene reservoir model, offshore East Kalimantan, Indonesia. American Association of Petroleum Geologists Bulletin 92, 919–949.

Schulz, M., Mudelsee, M., 2002. REDFIT: estimating red-noise spectra directly from unevenly spaced paleoclimate time series. Computer Geosciences 28, 421–426.

Scotchman, J., Pickering, K., Sutcliffe, C., Dakin, N., Armstrong, E., 2015. Milankovitch cyclicity within the middle Eocene deep-marine Guaso System, Ainsa Basin, Spanish Pyrenees. Earth-Science Reviews 144, 107–121.

Sømme, T.O., Helland-Hansen, W., Granjeon, D., 2009. Impact of eustatic amplitude variations on shelf morphology, sediment dispersal, and sequence stratigraphic interpretation: icehouse versus Greenhouse systems. Geology 37, 587–590.

Su, M., Lin, Z., Wang, C., Kuang, Z., Liang, J., Chen, H., Liu, S., Zhang, B., Luo, K., Huang, S., Wu, Q., 2020. Geomorphologic and infilling characteristics of the slope-confined submarine canyons in the Pearl River mouth basin, northern South China Sea. Marine Geology 424, 106166.

Sweet, M.L., Blum, M.D., 2016. Connections between fluvial to shallow marine environments and submarine canyons: implications for sediment transfer to deep water. Journal of Sedimentary Research 86, 1147–1162.

Sydow, J., Roberts, H.H., 1994. Stratigraphic framework of a late Pleistocene shelf-edge delta, northeast Gulf of Mexico. American Association of Petroleum Geologists Bulletin 78, 1276–1312.

Sylvester, Z., Deptuck, M.E., Prather, B.E., Pirmez, C., O'Byrne, C., 2012. Seismic stratigraphy of a shelf-edge delta and linked submarine channels in the northeastern Gulf of Mexico. In: Prather, B.E. (Ed.), Application of the Principles of Seismic Geomorphology to Continental-Slope and Base-of-Slope Systems: Case Studies from Seafloor and near-Sea Floor Analogues. vol. 99. SEPM Special Publication, Tulsa, Oklahoma, pp. 31–59.

Talling, P.J., Allin, J., Armitage, D.A., Arnott, R.W.C., Cartigny, M.J.B., Clare, M.A., Felletti, F., Covault, J.A., Girardclos, S., Hansen, E., Hill, P.R., Hiscott, R.N., Hogg, A.J., Hughes Clarke, J., Jobe, Z.R., Malgesini, G., Mozzato, A., Naruse, H., Parkinson, S., Peel, F.J., Piper, D.J.W., Pope, E., Postma, G., Rowley, P., Sguazzini, A., Stevenson, C.J., Sumner, E.J., Sylvester, Z., Watts, C., Xu, J., 2015. Key future directions for research on turbidity currents and their deposits. Journal of Sedimentary Research 85, 153–169.

Tripathi, S., Tiwari, M., Lee, J., Khim, B., IODP Expedition 355 Scientists, 2017. First evidence of denitrification visa-vis monsoon in the Arabian Sea since late Miocene. Scientific Reports 43056.

Vail, P.R., Mitchum, R.M., Thompson, S., 1977. Seismic stratigraphy and global changes of sea level, part 4, global cycles of relative changes of sea level. In: Payton, C.E. (Ed.), Seismic Stratigraphy, Application to Hydrocarbon Exploration. American Association of Petroleum Geologists Bulletinvol. 26, pp. 83–97.

Van Wagoner, J.C., Mitchum, R.M., Campion, K.M., Rahmanian, V.D., 1990. Siliciclastic sequence stratigraphy in well logs, cores, and outcrops: concepts for highresolution correlation of time and facies. American Association of Petroleum Geologists Bulletin 7, 55.

Vangriesheim, A., Khripounoff, A., Crassous, P., 2009. Turbidity events observed in situ along the Congo submarine channel. Deep-Sea Research 56, 2208–2222.

Wan, S., Li, A., Clift, P.D., Stuut, J.W., 2007. Development of the east Asian monsoon: mineralogical and sedimentologic records in the northern South ChinaSea since 20 Ma. Palaeogeography, Palaeoclimatology, Palaeoecology 254, 561–582.

Wang, Y.J., Cheng, H., Edwards, L.R., An, S.Z., Wu, Y.J., Shen, C., Dorale, A.J., 2001. A high-resolution absolute-dated late Pleistocene monsoon record from Hulu Cave, China. Science 294, 2345–2348.

Wang, X., Wang, Y., Tan, M., Cai, F., 2020. Deep-water deposition in response to sea-level fluctuations in the past 30 Kyr on the northern margin of the South China Sea. Deep-Sea Research Part I 163, 103317.

Wei, X., Wu, C.Y., 2011. Holocene delta evolution and sequence stratigraphy of the Pearl River Delta in SouthChina. Science China: Earth Sciences 54, 1523–1541.

Weimer, P., Slatt, R.M., 2007. Introduction to the Petroleum Geology of Deep-Water Settings. American Association of Petroleum Geologists, Studies in Geologyvol. 57 pp. 57–111.

Xie, Z., Sun, L., Pang, X., Zheng, J., Sun, Z., 2017. Origin of the Dongsha event in the south China sea. Marine Geophysical Research 38, 357–371.

Yao, B.C., 1999. Tectonic characteristics of northwest subbasin and seafloor spreading history of South China Sea in Cenozoic. Tropic Oceanology 18, 7–15 (in Chinese with English Abstract).

Yao, B.C., Yang, M., 2008. Tectonic movements in the late Cenozoic and gas hydrate resources in the South China Sea. Marine Geology & Quaternary Geology 28, 93–100 (in Chinese with English Abstract).

Zhang, S., Lu, X., Higgitt, D.L., Chen, C.-T.A., Han, J., Sun, H., 2008. Recent changes of water dischargeand sediment load in the Zhujiang (Pearl River) Basin,China. Global and Planetary Change 60, 365–380.

Zhang, J., Steel, R., Olariu, C., 2017. What conditions are required for deltas to reach the shelf edge during rising sea level? Geology 45, 1107–1110.

Zhang, J., Wu, S., Hu, G., Fan, T., Yu, B., Lin, P., Jiang, S., 2018. Sea-level control on the submarine fan architecture in a deepwater sequence of the Niger Delta Basin. Marine and Petroleum Geology 94, 179–197.

Zhao, S.J., Wu, S.G., Shi, H., Dong, D., Chen, R., Wang, Y., 2012. Structures and dynamic mechanism related to the Donghsa movement at the northern margin of South China Sea. Progress in Geophysics 27, 1008–1019.

Zhao, F., Alves, T.M., Wu, S., Li, W., Huuse, M., Mi, L., Sun, Q., Ma, B., 2016. Prolonged post-rift magmatism on highly extended crust of divergent continental margins (Baiyun Sag, South China Sea). Earth and Planetary Science Letters 445, 79–91.

Zhao, S., Liu, Z., Chen, Q., Wang, X., Shi, J., Jin, H., Liu, J., Jian, Z., 2017. Spatiotemporal variations of deep-sea sediment components and their fluxes since the last glaciation in the northern South China Sea. Science China: Earth Sciences 60, 1368–1381.

Zhu, M., Graham, S., Pang, X., McHargue, T., 2010. Characteristics of migrating submarine canyons from the middle Miocene to present: implications for paleoceanographic circulation, northern South China Sea. Marine and Petroleum Geology 27, 307–319.

Zhuo, H., Wang, Y., Shi, H., He, M., Chen, W., Li, H., Wang, Y., Yan, W., 2015. Contrasting fluvial styles across the mid-Pleistocene climate transition in the northern shelf of the South China Sea: evidence from 3D seismic data. Quaternary Science Reviews 129, 128–146.

Zong, Y., Lloyd, M.J., Leng, J.M., Yim, S.W., Huang, G., 2006. Reconstruction of Holocene monsoon history form the Pearl River Estuary, southern China, using diatoms and carbon isotope ratios. The Holocene 16, 251–263.